

**Synoptic Control over Orographic
Precipitation Distributions During
OLYMPEX**

David Purnell

**Atmospheric and Oceanic Sciences,
McGill University, Montreal**

June 2017

A thesis submitted to McGill University in partial fulfillment of
the requirements of the degree of Master of Science

©David Purnell 2016

Abstract

During the Olympic Mountains Experiment (OLYMPEX) in Washington State in winter 2015-16, intensive precipitation and upper-air measurements were obtained within frontal systems traversing the Olympic mountain range. In this study, an analysis and interpretation of the observed precipitation distributions, as a function of synoptic conditions, is undertaken. The synoptic conditions are categorized as warm-frontal (ahead of a surface warm front), warm-sector (between the surface warm and cold fronts), and post-frontal (behind the surface cold front). Six periods of each frontal class are selected, for which observed precipitation distributions are retrieved using a combination of operational S-band radars and a relatively dense regional rain-gauge network. Radar and rain gauge data is merged using a unique combination of bias correction and optimal estimation techniques. Not surprisingly, far greater orographic precipitation amounts are observed during warm-frontal and warm-sector periods than during post-frontal periods. The warm-sector periods exhibit the largest orographic enhancement directly over the massif, the warm-frontal periods exhibit a smaller enhancement over a large area upstream of the mountain and the post-frontal periods are characterised by a local maximum at the foot of the mountain. Analysis of upstream soundings indicates that the upstream shift of precipitation in warm frontal and postfrontal conditions is associated with a large nondimensional mountain height, suggesting strong upstream blocking. To enhance the physical interpretation, quasi-idealized simulations with the Weather Research and Forecasting (WRF) model are conducted. The simulations use the real Olympics terrain and idealized soundings based on the upper-air observations. Crucially, upstream precipitation (an element often missing from idealized orographic precipitation simulations) is considered by applying a large-scale lifting profile in the warm-frontal and warm-sector simulations, or by producing oceanic cellular convection upstream of the Olympics for the post-frontal simulations. Key differences between observed frontal periods are reproduced by the simulations. Sensitivity tests of upstream precipitation indicate that while the structure of the orographic enhancement fundamentally changes when upstream precipitation is included, the degree of orographic enhancement is not strongly dependent on the intensity of the upstream precipitation.

Abrégé

Durant les expériences des montagnes olympiques (Olympic Mountains Experiment, OLYMPEX) dans l'État de Washington à l'hiver 2015-16, des précipitations soutenues ainsi que des mesures aérologiques furent obtenues au sein des systèmes frontaux traversant la chaîne de montagnes Olympiques. Dans cette étude, une analyse et une interprétation des distributions de précipitation observée en tant que fonction de conditions synoptiques sont entreprises. Les conditions synoptiques sont classées ainsi: chaud-frontal (devant le front-chaud), secteur-chaud (entre les fronts chauds et froids) et post-frontale (derrière le front froid). Six cycles de chacune des classes frontales sont sélectionnés, où les distributions de précipitations sont obtenues grâce à des radars opérationnels S-Band et un réseau relativement dense de pluviomètres régionale. Sans surprise, une bien plus grande quantité de précipitations orographiques fut observée durant les périodes frontaux-chauds et secteurs-chaud plutôt que durant les périodes post-frontales. Les périodes de secteurs-chauds présentent les augmentations orographiques les plus grandes au-dessus de la montagne, les périodes frontaux-chauds présentent une augmentation plus petite dans une zone plus grande en amont de la montagne, et les périodes post-frontales sont caractérisées par les maximums locaux obtenus au bas du massif. Pour approfondir l'interprétation physique, des simulations quasi-idéalisées avec le modèle Weather Research and Forecasting (WRF) sont entreprises. Les simulations se fondent sur le terrain actuel de la chaîne de montagnes Olympiques et les sondages idéalisés sont basés sur les observations aérologiques. Il est important de souligner que les précipitations en amont (un élément souvent manquant des simulations de précipitations orographiques idéalisées) sont prises en compte en appliquant un rehaussement de profil de levage dans les simulations des frontaux-chauds et secteur-chaud, ou en produisant une convection océanique en amont des Olympiques pour les simulations post-frontales. Les différences marquantes entre les périodes frontales observées sont reproduites dans les simulations. Malgré l'inclusion du changement fondamental de la structure des augmentations orographiques, des essais de sensibilité des précipitations en amont indiquent que le degré d'augmentation orographique n'est pas fortement dépendant de l'intensité des précipitations en amont.

Acknowledgements

Firstly, I would like to thank Daniel Kirshbaum for his supervision and guidance during this project. Thanks to MEOPAR for providing the funding for my research. I would also like to express my gratitude to all those involved in data collection during OLYMPEX. Joe Zagrodnik provided me with invaluable information regarding the OLYMPEX rain gauge network and Jonathan Doyle helped with data acquisition. Thanks to Frédéric Fabry for his radar-related advice. Olly Osborne has been a consistent source of wisdom in regards to many aspects of this project. Thanks to Louis-Philippe Trépanier for his help with the Abrégé. I am extremely grateful for my friends and family for their consistent support, especially from my parents.

Contents

List of Figures	vi
List of Tables	ix
1 Introduction	1
1.1 Background	1
1.1.1 The Olympics	1
1.2 Orographic precipitation in midlatitudes	6
1.2.1 Overview	6
1.2.2 Observations	7
1.2.3 Modelling	9
1.3 Quantitative precipitation estimation	10
1.3.1 Measurements of precipitation	10
1.3.2 Radar and rain gauge merging techniques	12
1.4 OLYMPEX	13
1.5 Research Objectives	14
2 Observations	16
2.1 Introduction	16
2.2 Classification of frontal periods	16
2.3 Measurements of precipitation	21
2.3.1 Rain gauges	21
2.3.2 Radar	22
2.4 Radar and rain gauge merging	26
2.4.1 Mean field bias correction	27
2.4.2 Variational adjustment	28
2.4.3 Verification of MFB-2DVAR method	30
2.5 Results	33
2.5.1 Quantitative diagnostics	34
2.6 Discussion	40
3 Modelling	42
3.1 Introduction	42
3.2 Numerical setup	43
3.2.1 General	43
3.2.2 Warm-frontal	44
3.2.3 Warm-sector	46
3.2.4 Post-frontal	47
3.3 Simulations	49
3.4 Results	51
3.4.1 Comparison with observations	51

3.4.2	Sensitivity to upstream precipitation	55
3.5	Discussion	59
4	Conclusions	62
4.1	Future Work	64
	Bibliography	65

List of Figures

1.1	(a) Terrain height in the Olympics and (b) an estimate of the mean annual precipitation from 1981-2010 (PRISM Climate Group, Oregon State University, http://prism.oregonstate.edu). The black contours in (b) show the coastline and terrain height in intervals of 1km. The same contours are used repeatedly in Figures henceforth.	2
1.2	Idealized structure of an extratropical cyclone that passes the Olympics. The prefrontal section is synonymous with the warm-frontal section discussed in this study. Taken from Houze et al. (2017).	4
1.3	Example soundings taken from site ‘NPOL/D3R’ (marked on Figure 1.7) during (a) warm-frontal, (b) warm-sector and (c) post-frontal synoptic conditions. The soundings were chosen based on the methods described in Section 2.2. (OLYMPEX, NASA, http://olympex.atmos.washington.edu).	5
1.4	Vertical cross section with vertical velocity (contours of 0.86ms^{-1}) and snow mixing ratio (shaded contours of 0.01g kg^{-1}) from a simulation of stable flow over an idealized mountain. Taken from Jiang and Smith (2003).	7
1.5	Illustration taken from Peterson et al. (1991), of a vertical cross section through a mountain with a small amount of blocked flow (top) and a large amount of blocked flow (bottom). The terrain is bounded by a solid contour with hatching, the blocked flow is indicated by the shaded area bounded by a dashed contour and the lines with arrows are streamlines. Note that in the case of the large amount of blocked flow, the air begins to ascend further upstream of the mountain, hence the cloud extends further upstream.	8
1.6	Idealized Vertical Profile of Reflectivity (VPR) in stratiform precipitation. The 0°C isotherm is represented by the upper blue dashed line. The middle layer, where melting snow is being sampled, corresponds to the bright band. This local maximum in reflectivity occurs due to the microphysical properties of melting snow.	12
1.7	The OLYMPEX observational network. From Houze et al. (2017).	14
2.1	Locations of rain gauges, radars and radiosonde sites used in this study imposed on the terrain height. Radiosonde sites are labelled NPOL, UIL (Quillayute) and UVic (University of Victoria). KLGX and KATX are the abbreviations for the Langley Hill and Camano WSR-88D radars. QV refers to the Quinault Valley area, where several OLYMPEX gauges were installed. WS refers to the western slopes, where there is only one gauge covering a large area.	17

2.2	Examples of the surface analysis data from the WPC (http://www.wpc.ncep.noaa.gov/archives/web_pages/sfc/sfc_archive.php) used for the classification of frontal periods. (a) was used to classify the third warm-frontal period (WF3), (b) used to classify the third warm-sector period (WS3) and (c) was used to classify the second post-frontal period (PF2).	18
2.3	Radiosonde data from the station marked NPOL in Figure 2.1 (retrieved from http://olympex.atmos.washington.edu). (a) was used to classify the third warm-frontal period (WF3), (b) used to classify the third warm-sector period (WS3) and (c) was used to classify the second post-frontal period (PF2).	19
2.4	Radar PPI scans from the radar marked KLGX in Figure 2.1 (retrieved from http://olympex.atmos.washington.edu). (a) was used to classify the third warm-frontal period (WF3), (b) used to classify the third warm-sector period (WS3) and (c) was used to classify the second post-frontal period (PF2).	20
2.5	Correction added to radar data at each azimuth and range bin of the lowest elevation angle (0.5°) PPI scan for (a) the Camano and (b) the Langley Hill WSR-88D radars, due to partial blockage by terrain.	24
2.6	The height of the lowest unblocked radar beam interpolated to a common grid over the Olympics. The jumps in height are due to the lowest elevation angle being blocked by terrain and the next elevation angle being used. The stars indicate the location of the radars. The x and y axes indicate the distance, in km, away from a central point in the Olympics. These axes are used henceforth.	25
2.7	(a) Radar estimate of precipitation accumulation on the 3rd of December from 0600 to 1200 UTC (WF3) and (b) gauge measurements for the same period.	26
2.8	Areas of the domain in which MFB correction factors are calculated. KLGX1 and KLGX2 refer to the area of the domain covered by lowest and the second lowest elevation angle PPI scan of the KLGX radar labelled in Figure 2.1. KATX1, KATX2.1 and KATX2.2 refer to the area of the domain covered by lowest and the second lowest elevation angle PPI scan of the KLGX radar labelled in 2.1. UPPER is an additional area in the middle of the Olympics that is treated separately, covered by both KLGX and KATX radars.	28
2.9	(a) Estimate of precipitation following MFB adjustment, (b) estimate of precipitation before MFB adjustment, (c) the difference between (a) and (b), (d) rain gauge measurements, for the WF3 period described in table 2.1.	29
2.10	(a) Estimate of precipitation following 2DVAR adjustment, (b) estimate of precipitation before 2DVAR adjustment, (c) the difference between (a) and (b), (d) rain gauge measurements, for the WF3 period described in table 2.1.	31
2.11	(a) Estimate of precipitation following MFB-2DVAR adjustment, (b) Stage IV estimate of precipitation, (c) the difference between (a) and (b), for the WF3 period defined in Table 2.1.	33

2.12	Mean distribution of hourly precipitation rate following the MFB-2DVAR method for (a) warm-frontal, (b) warm-sector and (c) postfrontal periods during OLYMPEX. The distributions are the mean of the hourly precipitation rate for the six periods of each of the frontal classes shown in Table 2.1.	35
3.1	Terrain height and land use for the domain used in simulations. The blue represents the area that is treated as ocean.	44
3.2	An idealized sounding used to initialize warm-frontal simulations, with $z_{inv}=2\text{km}$. The number of lines on the tails of the wind barbs represent a wind speed of 10ms^{-1} each and the solid black triangle represents 50ms^{-1} . The solid black line is the temperature profile and the blue line is the dew point temperature.	46
3.3	Idealized sounding used to initialize warm-sector simulations. The wind barbs and the temperature profiles are as explained in the caption of Figure 3.2.	47
3.4	Idealized sounding used to initialize post-frontal simulations. The wind barbs and the temperature profiles are as explained in the caption of Figure 3.2.	48
3.5	Simulated radar reflectivity for: (a) the wf-control case with $z_{inv} = 2\text{km}$ at 4.5 hours into the simulation, (b) the ws-control case at the same time into the simulation, (c) one of the pf-control simulations at 9 hours. The times are chosen because they are half way into the respective periods that are used to calculate the mean hourly precipitation distribution. Here and henceforth, the black contours in the figures from simulations show the coastline and terrain height in intervals of 1km.	50
3.6	Mean hourly precipitation distribution for simulated (left column) and observed (right column) frontal periods over the Olympics. This data is obtained from (a) the wf-control simulations, (b) the warm-frontal observations, (c) the ws-control simulation, (d) the warm-sector observations, (e) the pf-control simulations and (f) the post-frontal observations. Figures (b), (d) and (f) are the same as Figures 2.12(a) (b) and (c), respectively.	54
3.7	Mean upstream precipitation (R_{up}) subtracted from the mean precipitation distributions for (a) wf-control, (b) ws-control and (c) pf-control.	55
3.8	Mean hourly precipitation distribution for warm-frontal and warm-sector simulations with varying values of w_{max} . The figures are ordered such that $w_{max} = 0\text{ms}^{-1}$ for the top row with (a) wf-wm0 and (b) ws-wm0, $w_{max} = 0.2\text{ms}^{-1}$ for the middle row with (c) wf-wm0.2 and (d) ws-control, and $w_{max} = 0.3\text{ms}^{-1}$ for the bottom row with (e) wf-control and (f) ws-wm0.3.	58
3.9	Mean hourly precipitation distribution for the pf-noflux simulations.	59

List of Tables

2.1	Frontal periods during OLYMPEX identified for use in this study. The periods are labelled by warm-frontal (WF), warm-sector (WS), post-frontal (PF) and a number to denote the order of occurrence within each frontal class. Note that all WF and WS periods are consecutive. During periods marked *, radiosonde data from the NPOL site was not available and data from the Quillayute site (UIL) was used instead (see Figure 2.1).	21
2.2	NRMSD between the MFB-2DVAR and Stage IV estimates of precipitation for 6 hour periods during three warm-frontal, warm-sector and post-frontal periods in December 2015. The Frontal Period column refers to the periods from Table 2.1, in which the six hour periods are contained.	34
2.3	Soundings used for calculating upstream flow properties for the periods outlined in Table 2.1. The locations of the sites NPOL and UIL are marked on Figure 2.1.	36
2.4	Properties of the warm-frontal, warm-sector and post-frontal periods outlined in table 2.1 and the mean properties for each class; labelled WF, WS and PF respectively.	39
3.1	Details of the simulations discussed herein. The Fluxes entry refers to whether or not the surface fluxes and advective cooling outlined in Section 3.2.4 are being used. The Quantity entry refers to the number of simulations that are averaged for each case.	49
3.2	Mean properties of observed and simulated frontal periods. wf-obs, ws-obs and pf-obs refer to the mean observed warm-frontal, warm-sector and post-frontal periods from Chapter 2, respectively.	52
3.3	The same as in Table 3.2 but with properties from the additional simulations outlined in Table 3.1.	56

Chapter 1

Introduction

1.1 Background

1.1.1 The Olympics

The Olympic Peninsula in Washington State consists of a roughly 100km wide, quasi-circular mountain range (shown in Figure 1.1(a)) that has an unusually wet and temperate climate. The southwest facing slopes host one of the few midlatitude rain forests in the world (the Hoh Rain Forest), which receives approximately 3,300mm of precipitation per year, in comparison with 900mm nearby in Seattle (WRCC, 2017). The sharp gradients in the annual precipitation over the isolated complex terrain, as shown in Figure 1.1(b) (an estimate of annual precipitation that is interpolated from a sparse set of surface measurements), make the Olympics an ideal natural laboratory for the study of midlatitude orographic precipitation.

The majority of precipitation in the Olympics is produced by the interaction of the complex terrain with extratropical cyclones that develop over the Pacific Ocean. A mature extratropical cyclone that typically transits this region consists of distinct sectors that are bounded by surface fronts, as shown in Figure 1.2 (e.g., Houze and Hobbs, 1982; Medina et al., 2007; Nagle and Serebreny, 1962). In the warm-frontal zone, ahead of the surface warm front, the mean flow direction is south-southwesterly and stratiform precipitation is observed as a warm air mass ascends slantwise over a cooler air mass. The warm-frontal zone is manifested in the vertical as a largely saturated layer with

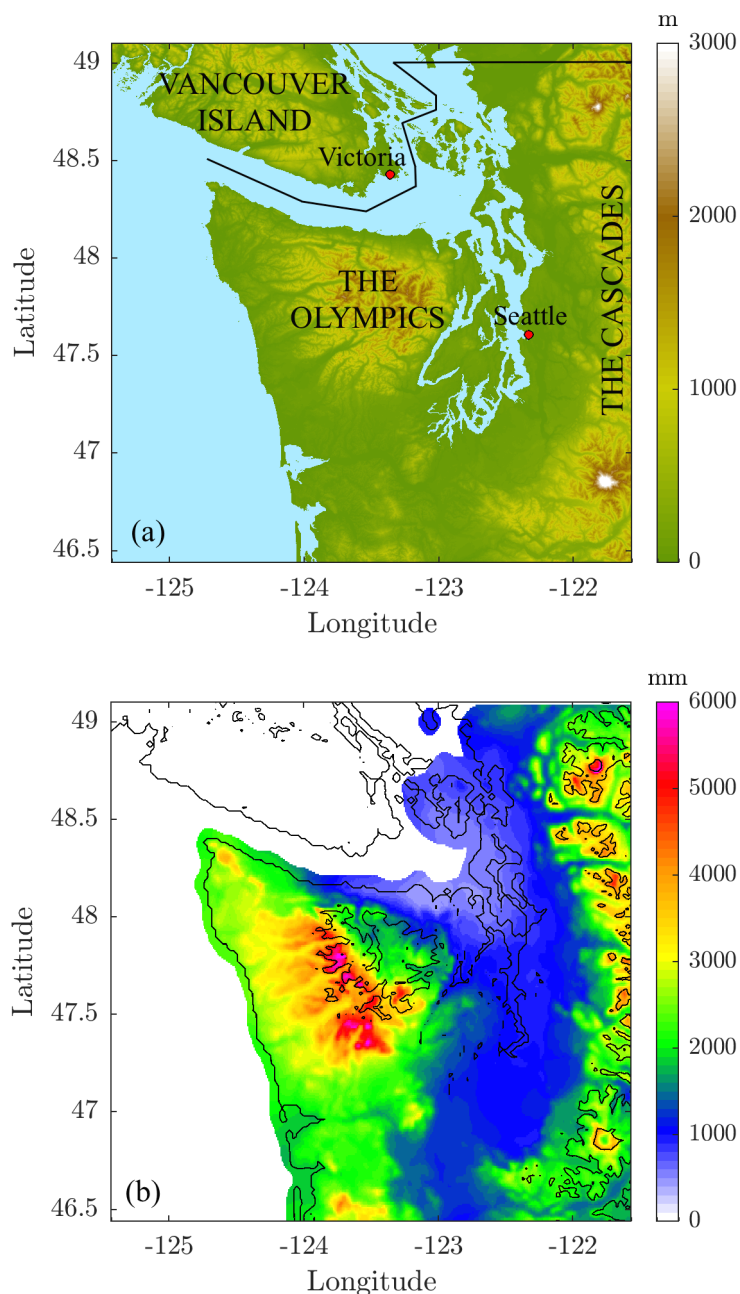


Figure 1.1: (a) Terrain height in the Olympics and (b) an estimate of the mean annual precipitation from 1981-2010 (PRISM Climate Group, Oregon State University, <http://prism.oregonstate.edu>). The black contours in (b) show the coastline and terrain height in intervals of 1km. The same contours are used repeatedly in Figures henceforth.

veering winds (consistent with strong warm air advection), that is topped by an often sharp frontal inversion. Figure 1.3(a) is a real-world example of a sounding observed prior to the passage of a surface warm front, in which the frontal inversion is evident between 850-825hPa. The warm-sector follows the passage of the surface warm front and is characterized by a warm air mass that is bounded either side by a cooler air mass (at the surface these boundaries are the warm and cold fronts). The flow is largely saturated and exhibits a nearly pseudoadiabatic temperature profile. The vertical wind profile is more

uniform and westerly, with a large water vapour flux that often meets the conditions to be classified as an atmospheric river (Neiman et al., 2008; Zhu and Newell, 1998). A real-world example of a sounding observed in a warm-sector is shown in Figure 1.3(b). In the post-frontal sector, following the passage of a surface cold front, the wind speed is slower and turns to west-northwesterly. The lowest layer of the atmosphere is drier than in the warm-sector and conditionally unstable, which permits the production of convective cells. A real-world example of a sounding taken following the passage of a cold front is shown in Figure 1.3(c), in which the conditional instability is evident between 975-850hPa.

Given the reliability of frontal systems traversing the complex terrain and producing heavy precipitation, the Olympics have been the focus of numerous studies (e.g., Anders et al., 2007; Colle and Mass, 1996; Ferber and Mass, 1990; Mass and Ferber, 1990; Minder et al., 2008; Parsons and Hobbs, 1983). Notable field experiments include the fourth intensive observing period during the Coastal Observation and Simulation with Topography (COAST IOP 4) field experiments (Colle and Mass, 1996), in which the interaction between low-level southwesterly flow and the Olympic mountains was investigated, and the Olympex field experiment (Ferber and Mass, 1990; Mass and Ferber, 1990) (not to be confused with the OLYMPEX campaign that is a focus of this thesis), in which pressure perturbations around the Olympics were studied for numerous flows with varying characteristics.

Whilst the basic mechanisms that produce the distribution of precipitation shown in Figure 1.1(b) are well known (as will be discussed in the next section), the distributions of precipitation that are produced by the background synoptic conditions have not been extensively studied.

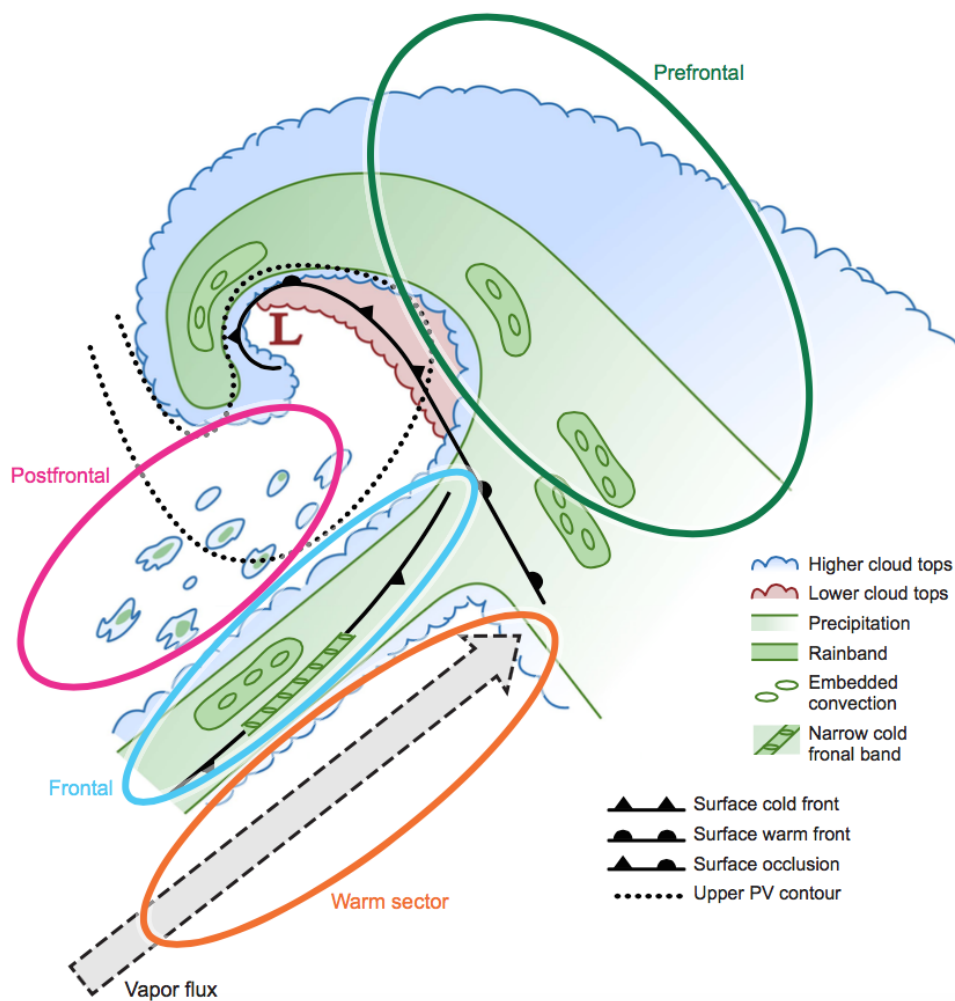


Figure 1.2: Idealized structure of an extratropical cyclone that passes the Olympics. The prefrontal section is synonymous with the warm-frontal section discussed in this study. Taken from Houze et al. (2017).

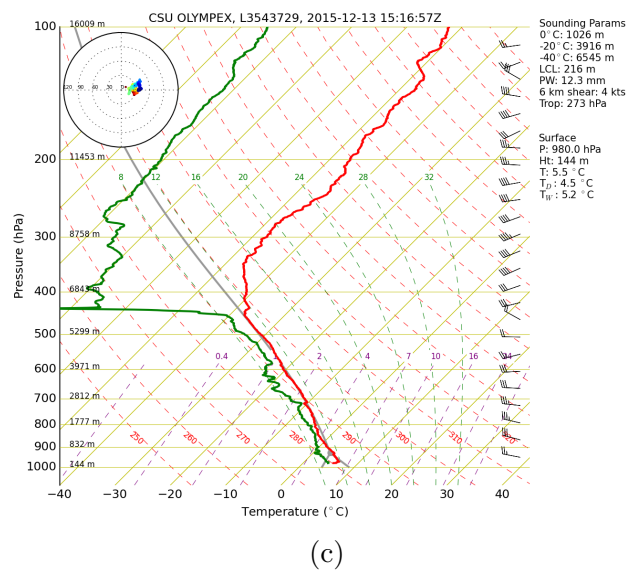
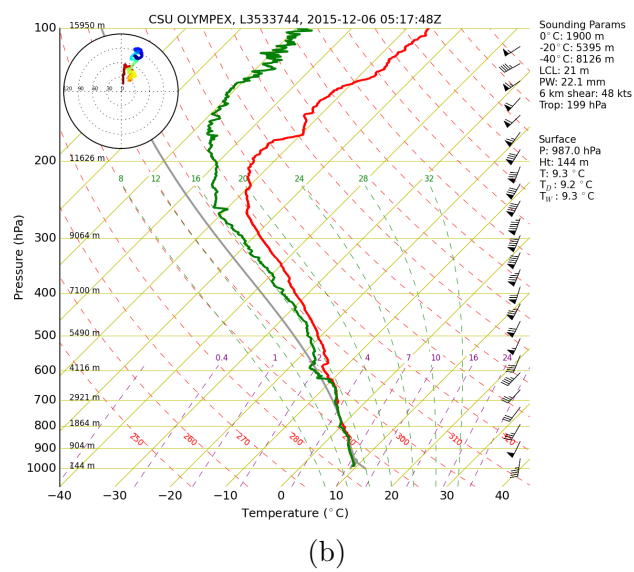
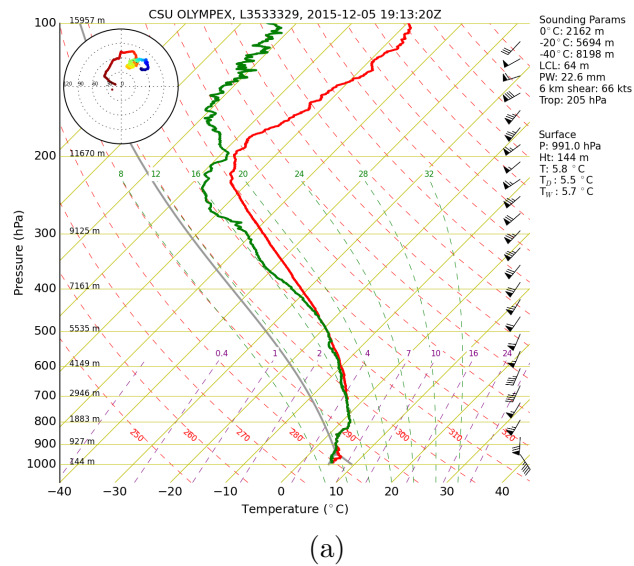


Figure 1.3: Example soundings taken from site ‘NPOL/D3R’ (marked on Figure 1.7) during (a) warm-frontal, (b) warm-sector and (c) post-frontal synoptic conditions. The soundings were chosen based on the methods described in Section 2.2. (OLYMPEX, NASA, <http://olympex.atmos.washington.edu>).

1.2 Orographic precipitation in midlatitudes

1.2.1 Overview

The estimate of the annual precipitation shown in figure 1.1(b) can be partially explained using basic physical arguments (e.g., Houze, 2012), given the mean southwesterly flow over the Olympics. Firstly, consider a moist stable flow with strong enough cross-barrier winds such that the near surface air is forced to ascend the slopes of a mountain (or synonymously, an unblocked flow). In this case, gravity waves will propagate vertically in response to the negative buoyancy generated by adiabatic ascent of stably-stratified flow over the terrain and precipitating clouds will form as the air is brought to saturation and condenses on the windward facing slopes. The precipitating clouds will then dissipate on the lee-side of the mountain as the air descends and the condensed water evaporates (e.g., Durran and Klemp, 1983). An example of this is shown Figure 1.4, in which a large cloud can also be seen aloft over the lee slope, due to a vertically propagating gravity wave. Convective precipitation may also occur in response to a potentially unstable air flow ascending the slopes of a mountain. Furthermore, the seeder-feeder mechanism accounts for enhanced precipitation on the windward slopes of a mountain. This occurs when precipitation from a cloud over a mountain falls through a lower-level orographically forced cloud and grows by collision and coalescence or accretion (e.g., Bader and Roach, 1977).

The response of a continuously stably stratified airflow of uniform cross-barrier wind speed encountering a mountain can be predicted using the nondimensional mountain height $\epsilon = Nh_0/U$, where N is the impinging Brunt-Väisälä frequency, U is the impinging cross-barrier flow speed and h_0 is the peak height of the mountain. To obtain linear solutions of mountain airflows, an underlying assumption is that the flow ascends the slopes of the mountain, but for flows with $\epsilon \gg 1$, linear theory is no longer valid (e.g., Smith, 1990). Instead, the flow tends to stagnate on the windward slopes and is diverted horizontally around the mountain. The stagnating flow acts as a barrier such that the flow starts to ascend upstream of the mountain, which causes an upstream shift of precipitation. In this case, the flow is referred to as being blocked by the terrain (see

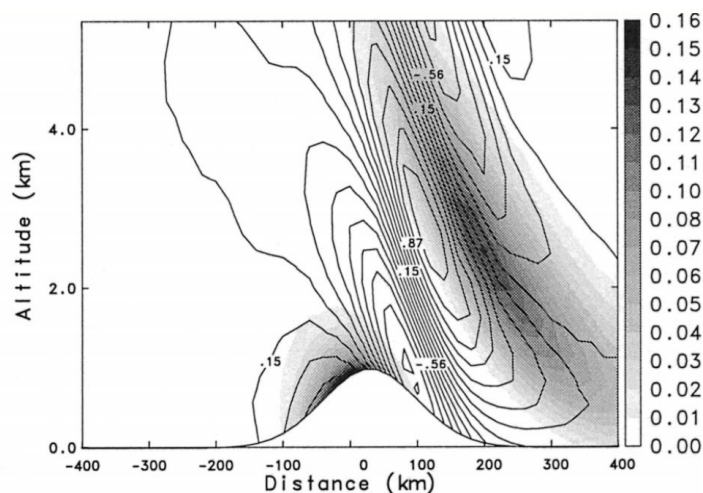


Figure 1.4: Vertical cross section with vertical velocity (contours of 0.86ms^{-1}) and snow mixing ratio (shaded contours of 0.01g kg^{-1}) from a simulation of stable flow over an idealized mountain. Taken from Jiang and Smith (2003).

Figure 1.5). ϵ has been shown to be a useful parameter for predicting topographic blocking through numerical simulations and observational studies (e.g., Houze et al., 2001; Jiang, 2003; Neiman et al., 2002; Ólafsson and Bougeault, 1996; Peterson et al., 1991). However, Reinecke and Durran (2008) found that ϵ has its limitations for predicting the onset of topographic blocking in realistic situations where the flow is not uniformly stratified in the vertical, because different methods for estimating N in the sub-crest layer produce significantly different results.

1.2.2 Observations

Numerous studies have observed the orographic modification of extratropical cyclones (e.g. Browning et al., 1974; Doyle and Bond, 2001; Hobbs, 1975; Parsons and Hobbs, 1983; Passarelli and Boehme, 1983). Passarelli and Boehme (1983) found that gauges on the windward slopes of the hills and small mountains in southern New England received 20-60% more precipitation during warm-frontal periods than those upstream in nearby coastal regions. Browning et al. (1974) studied the effect of the hills in southern Wales on a passing extratropical cyclone. In the warm-sector, they found that the rainfall over the hills was increased by a factor of six in comparison to an upstream coastal location, as opposed to a factor of three during the warm-frontal period. They attribute this large warm-sector enhancement to the presence of a layer of potential instability in

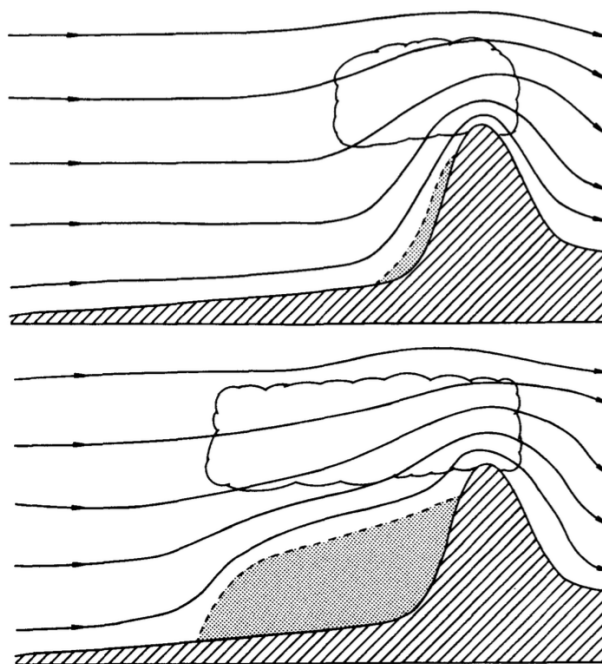


Figure 1.5: Illustration taken from Peterson et al. (1991), of a vertical cross section through a mountain with a small amount of blocked flow (top) and a large amount of blocked flow (bottom). The terrain is bounded by a solid contour with hatching, the blocked flow is indicated by the shaded area bounded by a dashed contour and the lines with arrows are streamlines. Note that in the case of the large amount of blocked flow, the air begins to ascend further upstream of the mountain, hence the cloud extends further upstream.

the middle troposphere, which permitted the development of an extra layer of clouds and hence enhancement by the aforementioned seeder-feeder effect. Recently, orographic enhancement of precipitation on the coast of California during atmospheric river events has received considerable attention (Neiman et al., 2014; Smith et al., 2010).

Rather than explicitly comparing between frontal periods, orographic precipitation events are often categorised according to whether the low-level flow is blocked or unblocked (which is strongly influenced by the background synoptic conditions). For example, Houze et al. (2001) found that there was an upstream shift of precipitation during blocked flow and significantly more orographic enhancement during unblocked flow encountering the Mediterranean side of the Alps during the Mesoscale Alpine Programme field campaign in 1999. Neiman et al. (2002) took a statistical approach to studying orographic precipitation in California and found a strong correlation between the magnitude of the cross-barrier (upslope) flow and rainfall rate measured in the mountains during unblocked flow, which was diminished near the surface when the low level flow was blocked.

Fewer observational studies of orographic modification of post-frontal precipitation exist than of warm-frontal and warm-sector, which is probably because the precipitation is generally much weaker under these conditions. Parsons and Hobbs (1983) observed convective rainbands generated following a passage over the Willipa and Black hills (relatively shallow hills to the south of the Olympics) during post-frontal conditions. They find that the contribution of precipitation during the post-frontal period relative to the accumulation for the entire frontal passage is much greater for the inland gauges than the coastal gauges, which they attribute to upslope flow ahead of the mountains. Kirshbaum and Durran (2005b) and Kirshbaum et al. (2007) observed convective rain bands over the Coastal Range in western Oregon and they used quasi-idealized numerical simulations to investigate the underlying dynamics.

1.2.3 Modelling

Numerical studies of orographic precipitation come in two forms: real-case simulations that use numerical weather prediction models and idealized simulations. Real-case simulations are either used to enhance the understanding of specific weather events (e.g., Buzzi et al., 1998; Colle and Mass, 1996; Medina and Houze, 2003; Steenburgh and Mass, 1996) or to verify models against observations (e.g., Anders et al., 2007; Colle and Mass, 2000; Cookson-Hills et al., 2017). Anders et al. (2007) used the Operational fifth-generation Pennsylvania State University–NCAR Mesoscale Model (MM5) to generate a fine-scale (4-km) precipitation climatology over the Olympics. A fine-scale climatology such as this is difficult to obtain using observations and possibly inaccurate, which is likely to be the case for the climatology shown in Figure 1.1(b) given that it is interpolated from a sparse set of surface observations (the difficulties associated with precipitation retrieval will be discussed in the next section). Whilst real-case simulations are useful, their complexity can limit general understanding of orographic precipitation processes.

Idealized numerical simulations permit the user to limit and control the parameters of interest, which may lead to a deeper understanding of orographic precipitation processes. Many have taken this approach to studying the interaction between an air flow and a mountain (e.g., Jiang, 2003; Kirshbaum and Smith, 2008; Ólafsson and Bougeault, 1996;

Siler and Durran, 2016). Jiang (2003) used models of varying complexity to show the extent to which latent heat release (due to condensation) assists low-level air in ascending the slopes of a mountain for a stably stratified flow. Recently, Siler and Durran (2016) investigated the occurrence of rain shadows to the lee of the Cascades using quasi-idealized simulations. They found that weak rain shadow events (i.e. events that did not exhibit a significant decrease in precipitation to the lee of the mountains) correlated with the passage of a warm front where there was a greater temperature difference between the air masses either side of the front (and therefore more veering of winds below the inversion). Cold air is trapped in the lee following the passage of the warm front, which suppresses the propagation of mountain waves and therefore also suppresses the leeside evaporation.

Despite the fact that most midlatitude orographic precipitation occurs in the context of precipitating synoptic-scale disturbances crossing the terrain, idealized simulations up to now have largely neglected the presence of upstream precipitation (with the notable exceptions of Kirshbaum and Durran (2005b), Kirshbaum and Grant (2012) and Richard et al. (1987)). The neglect of large-scale forcing (which is the cause of upstream precipitation) can result in large differences between idealized simulations and corresponding real scenarios, which limit the usefulness of the simulations in understanding reality. For example, if large-scale ascent is neglected in an idealized simulation of a warm-frontal or warm-sector period, upstream precipitation will not develop and the seeder-feeder process is inactive. Thus, the orographic cloud must generate its precipitation internally, which may greatly limit its precipitation efficiency.

1.3 Quantitative precipitation estimation

1.3.1 Measurements of precipitation

Accurate fine-scale ($O(1\text{km})$) precipitation fields are difficult to obtain, especially over complex terrain. Radars and rain gauges are the most popular precipitation measuring instruments but both are significantly flawed.

Rain gauges provide a direct measurement of precipitation accumulation but there are many issues associated with rain gauge networks. For example, it is impractical

to install and maintain gauges in remote locations or at high altitudes, which leads to sparse gauge networks in which gauges are preferentially installed in valleys. Anders et al. (2007) installed a dense gauge network across a 10km-wide ridge on the southwest slopes of the Olympics and found an increase of 50% annual precipitation on top of the ridge relative to the adjacent valleys. Variability of the precipitation phase over complex terrain also poses issues for rain gauges. This is primarily because rain gauges do not accurately measure precipitation when it is snowing. Yang et al. (1998) showed that the standard National Weather Service 8" gauges underestimated liquid equivalent snowfall by up to 55% over two winter seasons. The U.S. Department of Agriculture snowpack telemetry (SNOTEL) sites are an exception because they are equipped with a snow pillow that weighs the snowfall and converts it to equivalent water, but there are only four such stations in the Olympics (see Figure 1.7).

On the other hand, radars provide remote measurements over a relatively large area (often over a radius of more than 200km) and at a fine resolution (approximately 1km) but there are many sources of errors associated with precipitation retrieval (e.g., Fabry, 2015; Joss et al., 1990). Namely, radars do not directly measure the precipitation rate, instead they measure the reflectivity (and other parameters), which is proportional to the diameter (to the power of six) and the number concentration of the hydrometeors in the sampling volume. Converting reflectivity (Z) aloft to the precipitation rate (R) at the surface (this is referred to as a Z - R relationship) is nontrivial and often leads to large errors.

Precipitation retrieval using radar is further complicated over terrain due to beam blockage. This occurs when some part, or all, of the transmitted radiation from the radar is blocked by terrain, preventing the radar from seeing anything beyond it. For the operational S-band WSR-88D radars that take measurements over the Olympics (see figure 1.7), partial beam blockage can be accounted for by approximating the portion of the beam width that is blocked by terrain at each range bin and adjusting the reflectivity accordingly (e.g. Fulton et al., 1998). However, as the altitude of the radar beam increases with the range from the radar, the reflectivity may vary due to the change in phase of the precipitation around the freezing level, even if the precipitation rate at the surface

is horizontally uniform. This may lead to an overestimation of surface rainfall if melting snow is being sampled (this phenomenon is known as the bright band), or an underestimation if snow is being sampled (see Figure 1.6). By assuming a horizontally uniform vertical profile of reflectivity (VPR) it is possible to correct the data (e.g., Berenguer and Zawadzki, 2009). Unfortunately, such an assumption is not justified over the Olympics because of spatial variations in microphysical processes over complex terrain (e.g., Purdy et al., 2005).

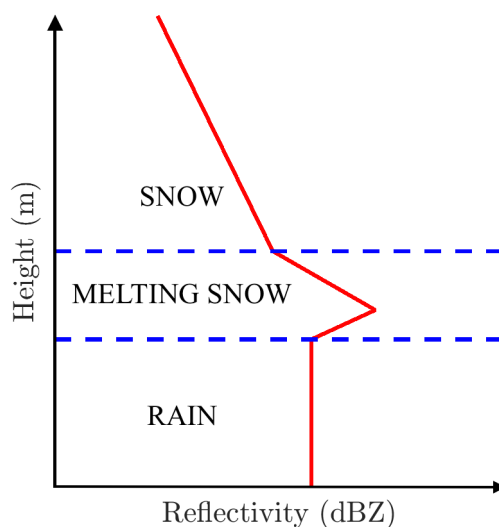


Figure 1.6: Idealized Vertical Profile of Reflectivity (VPR) in stratiform precipitation. The 0°C isotherm is represented by the upper blue dashed line. The middle layer, where melting snow is being sampled, corresponds to the bright band. This local maximum in reflectivity occurs due to the microphysical properties of melting snow.

1.3.2 Radar and rain gauge merging techniques

Neither radar nor rain gauge networks are individually sufficient to accurately produce fine-scale precipitation distribution data over complex terrain. Because these are complementary sources of data, radar and rain gauge merging is an active area of research. Several different methods of varying complexity exist (see Goudenhoofdt and Delobbe (2009) for a review). These methods can be loosely split into two categories: methods that use the gauge measurements to apply a single or multiple correction factors to the radar derived precipitation field and geostatistical methods that spatially interpolate the gauge data with some use of the radar data (e.g. Sideris et al., 2014; Sinclair and Pegram, 2005; Velasco-Forero et al., 2009). For this study we focus on the former of the

two categories.

Mean Field Bias correction (MFB) is a simple merging technique that is used operationally by the National Weather Service (Seo et al., 1999). This technique assumes that there is a uniform multiplicative error over the whole radar field, which could be due to radar miscalibration or use of an inaccurate Z - R relation. This method is limited in that it does not address sub domain-scale error (e.g., vertical profile of reflectivity (VPR) related errors or partial beam blockage). Therefore, more complex methods exist, such as range dependent adjustment (Koistinen and Michelson, 2002) and Brandes spatial adjustment (Brandes, 1975), which take into account some of these sources of errors.

More recently, Bianchi et al. (2013) presented a variational method to merge radar, rain gauges and microwave links. This is an optimal estimation approach, which depends on error covariance matrices that are constructed for each set of observations. The radar-derived precipitation field comprises the first guess, which is then modified by assimilation of the gauge data such that the error in close proximity to the gauges is greatly reduced. Another advantage of this method is that it can be relatively easily adapted to include multiple data sources, such as microwave links (Bianchi et al., 2013) or satellite and airborne radars. Following the success of the Tropical Rainfall Measurement Mission (Kummerow et al., 1998) and the subsequent launch of the Global Precipitation Measurement Mission (GPM) (Hou et al., 2014), satellites are certain to become more popular for operational precipitation retrieval. Therefore, the development and improvement of multi-sensor precipitation retrieval techniques is of crucial importance.

1.4 OLYMPEX

The Olympic Mountains Experiment (OLYMPEX) was a field campaign that took place from November 2015 to February 2016. The purpose of the campaign was twofold: to provide ground validation data for the GPM satellite mission and to measure orographic precipitation in the Olympics. As shown in Figure 1.7, various dual-polarization radars, research aircrafts and rain gauges were set up to obtain detailed atmospheric measurements during the passages of extratropical cyclones. This additional instrumentation, combined with pre-existing rain gauge networks and operational S-band WSR-88D radars,

provided an excellent opportunity to estimate the spatial distribution of precipitation over the Olympics during frontal passages. For more details about OLYMPEX, see the overview paper by Houze et al. (2017).

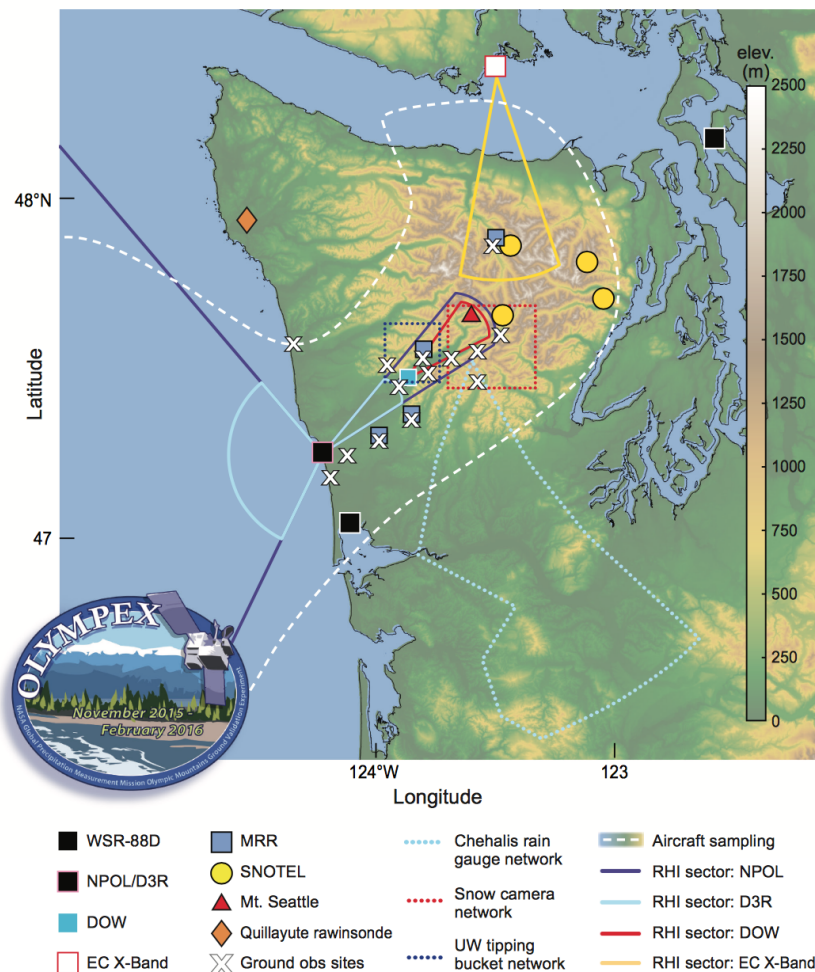


Figure 1.7: The OLYMPEX observational network. From Houze et al. (2017).

1.5 Research Objectives

The main objective of this study is to retrieve precipitation distributions over the Olympics during warm-frontal, warm-sector and post-frontal conditions, and analyze the differences between them. Due to the short length and complexity of the passages of cold fronts over the Olympics, they are not considered herein. Section 2 will focus on observations. Firstly, a method for retrieving precipitation distributions over the Olympics will be developed. Following the identification of six warm-frontal, warm-sector and post-frontal periods during OLYMPEX, the distribution for each frontal class over the six periods

will be presented and their differences will be quantified and discussed. Quasi-idealized numerical simulations of frontal periods over the Olympics terrain are presented in section 3. The simulations are compared to observations and some sensitivity tests of the upstream precipitation rate are conducted. Concluding remarks are given in section 4.

Chapter 2

Observations

2.1 Introduction

In this chapter, a technique for estimating the distribution of precipitation over the Olympics using radar and rain gauge data is outlined. This technique is subsequently used to estimate the distribution of precipitation during frontal periods, such that they can be compared against each other. We intend to evaluate the relationship between the precipitation distributions for each frontal class and basic properties of the upstream flow. The locations of the instruments used in this chapter are shown in Figure 2.1.

2.2 Classification of frontal periods

Six warm-frontal, warm-sector and post-frontal periods during OLYMPEX have been identified. These periods were identified primarily based on surface analysis maps provided by the NWS Weather Prediction Center (WPC) (http://www.wpc.ncep.noaa.gov/archives/web_pages/sfc/sfc_archive.php). Radiosonde data (see stations in Figure 2.1) was also used to identify the following frontal features: a temperature inversion that bounds a warmer and cooler air mass and low-level warm air advection (veering winds) ahead of a warm surface front, a temperature profile that is nearly neutral to moist convection (or pseudoadiabatic) in the warm-sector, low-level cold air advection (backing winds) behind a cold front, instability near the surface in post-frontal conditions. Additionally, animations of radar Plan Position Indicator (PPI) scans from the

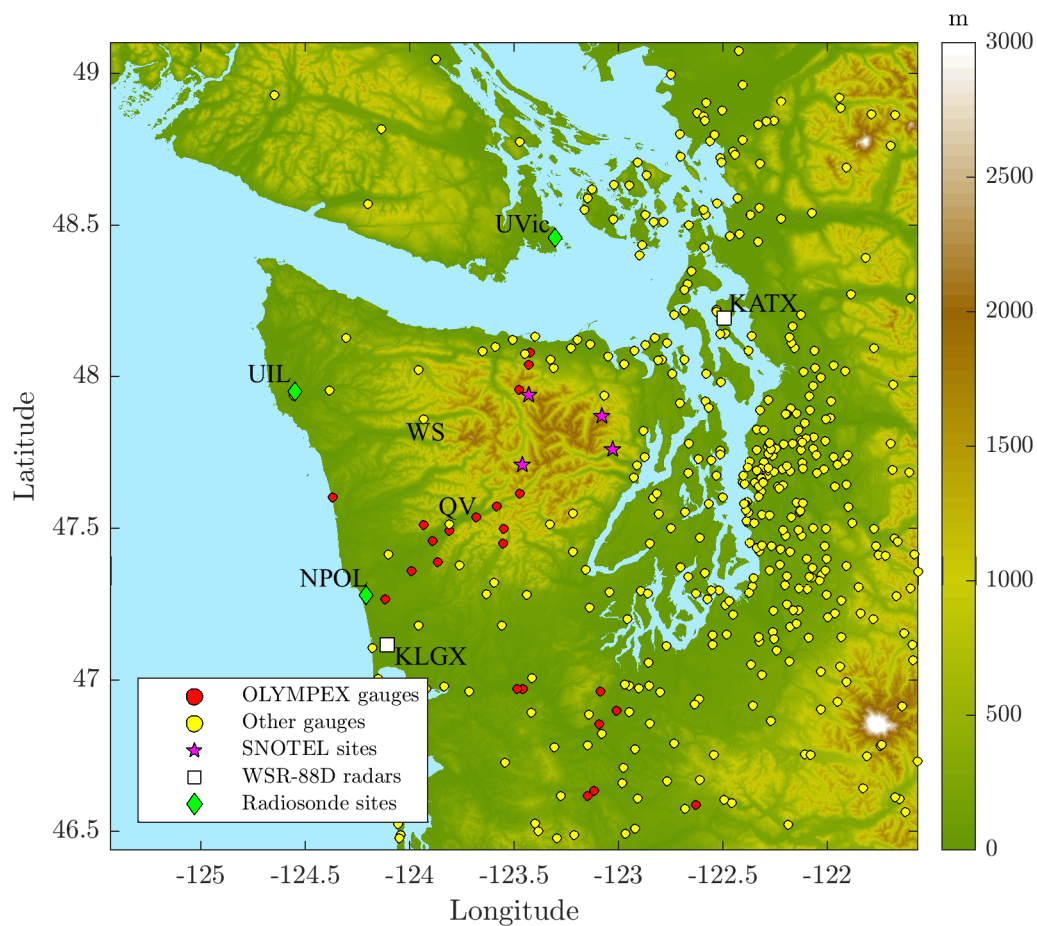
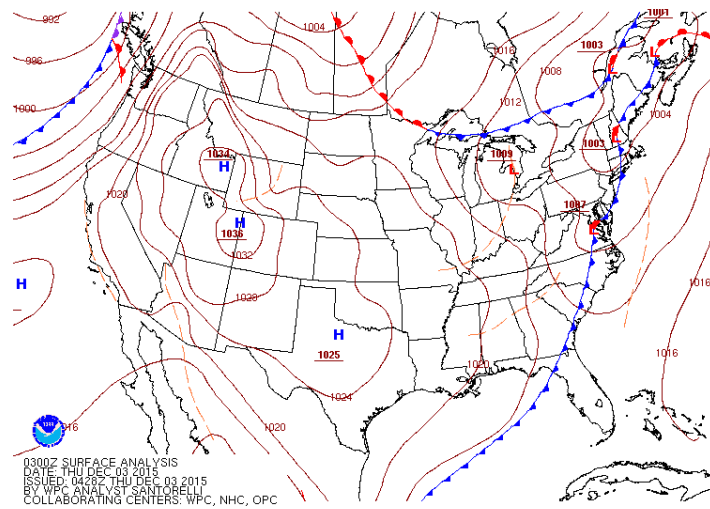
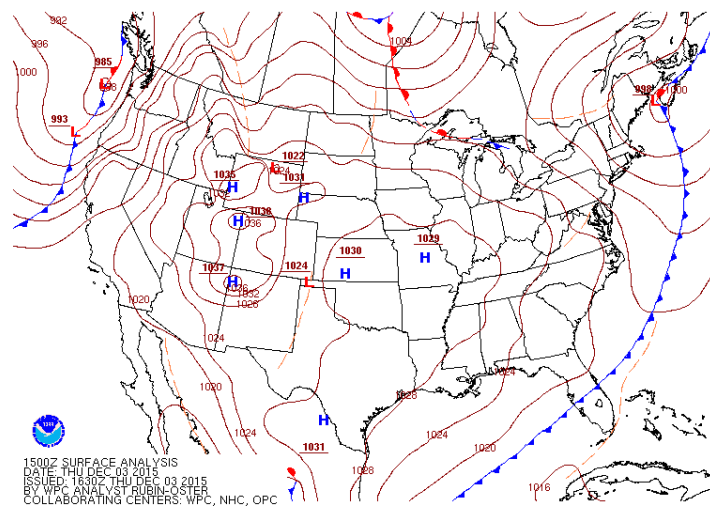


Figure 2.1: Locations of rain gauges, radars and radiosonde sites used in this study imposed on the terrain height. Radiosonde sites are labelled NPOL, UIL (Quillayute) and UVic (University of Victoria). KLGX and KATX are the abbreviations for the Langley Hill and Camano WSR-88D radars. QV refers to the Quinault Valley area, where several OLYMPEX gauges were installed. WS refers to the western slopes, where there is only one gauge covering a large area.

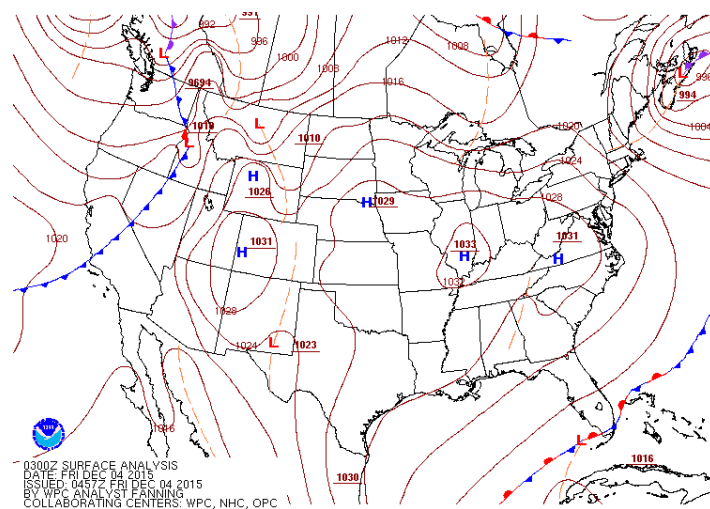
OLYMPEX website (<http://olympex.atmos.washington.edu>) were viewed for: stratiform and widespread precipitation in a warm-frontal period, ragged patches of precipitation in the warm-sector, a narrow band of heavy precipitation along a cold surface front, scattered and occasionally heavy precipitation in post-frontal periods (Nagle and Serebreny, 1962). Examples of the data used to classify frontal periods are shown in Figures 2.2, 2.3 and 2.4. The classified frontal periods are given in Table 2.1. Similar periods are also identified in Houze et al. (2017).



(a) 03 December 2015 at 0300UTC.

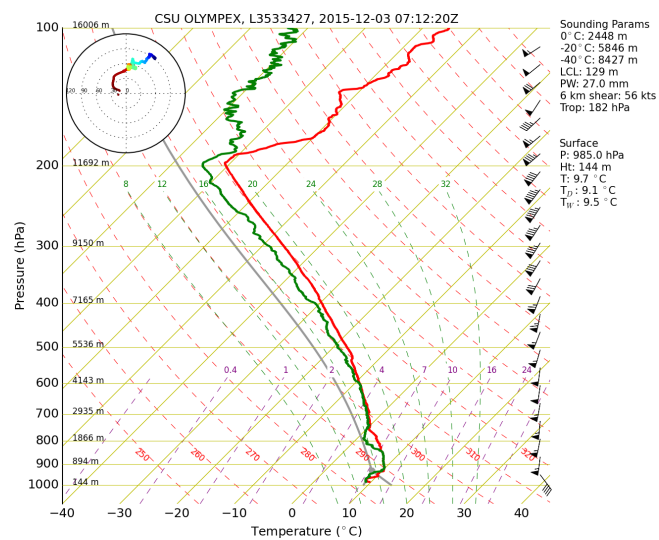


(b) 03 December 2015 at 1630UTC.

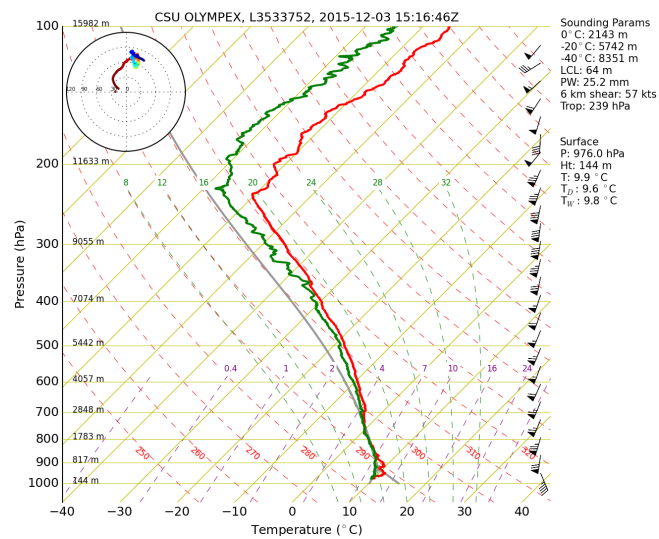


(c) 04 December 2015 at 0457UTC.

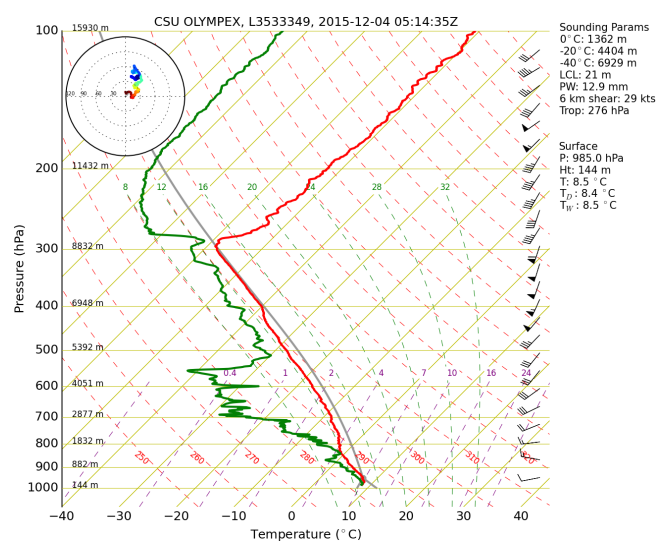
Figure 2.2: Examples of the surface analysis data from the WPC (http://www.wpc.ncep.noaa.gov/archives/web_pages/sfc/sfc_archive.php) used for the classification of frontal periods. (a) was used to classify the third warm-frontal period (WF3), (b) used to classify the third warm-sector period (WS3) and (c) was used to classify the second post-frontal period (PF2).



(a) 03 December 2015 at 0712UTC.

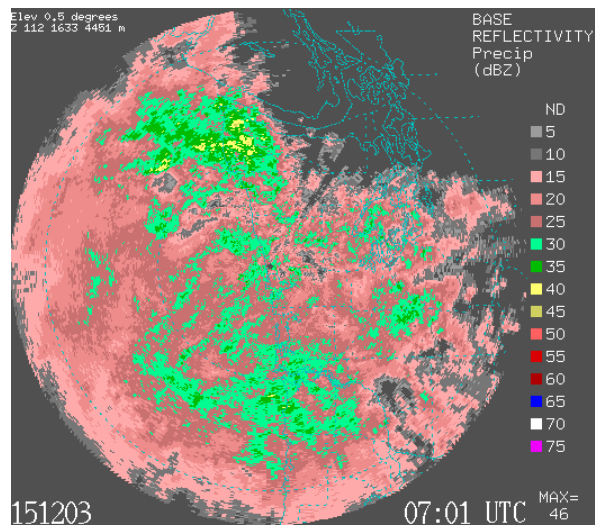


(b) 03 December 2015 at 1516UTC.

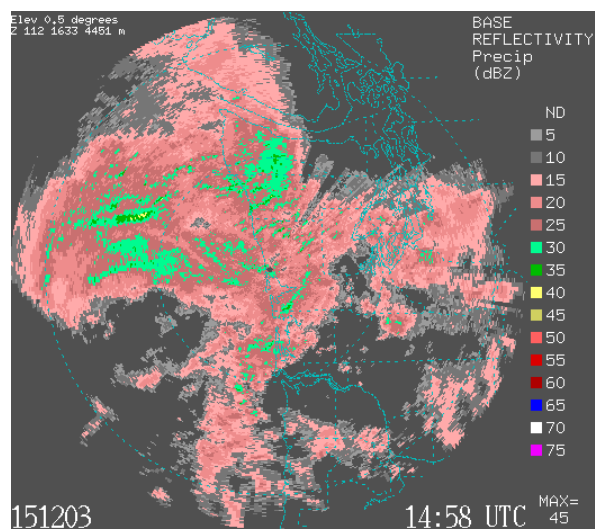


(c) 04 December 2015 at 0514UTC.

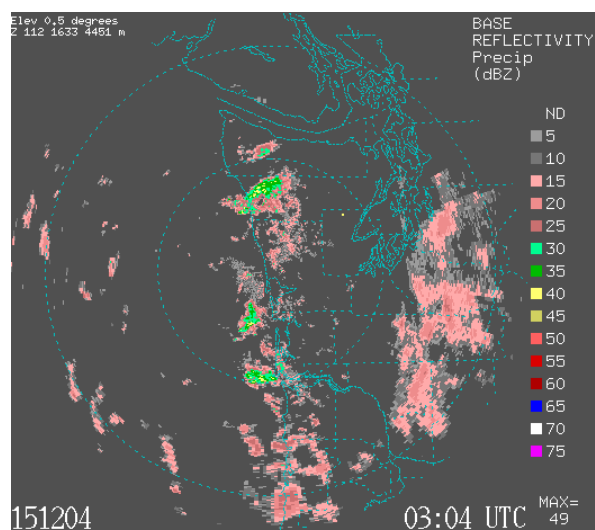
Figure 2.3: Radiosonde data from the station marked NPOL in Figure 2.1 (retrieved from <http://olympex.atmos.washington.edu>). (a) was used to classify the third warm-frontal period (WF3), (b) used to classify the third warm-sector period (WS3) and (c) was used to classify the second post-frontal period (PF2).



(a) 03 December 2015 at 0701UTC.



(b) 03 December 2015 at 1458UTC.



(c) 04 December 2015 at 0304UTC.

Figure 2.4: Radar PPI scans from the radar marked KLGX in Figure 2.1 (retrieved from <http://olympex.atmos.washington.edu>). (a) was used to classify the third warm-frontal period (WF3), (b) used to classify the third warm-sector period (WS3) and (c) was used to classify the second post-frontal period (PF2).

Period	Date	Time (UTC)
WF1	2015 Nov 12-13	1700-0300
WS1	2015 Nov 13	0300-1200
WF2	2015 Nov 16-17	1900-1000
WS2	2015 Nov 17	1000-1700
PF1	2015 Nov 18	0100-1900
WF3	2015 Dec 3	0600-1200
WS3	2015 Dec 3	1200-2100
PF2	2015 Dec 4-5	0500-0000
WF4	2015 Dec 5-6	1300-0000
WS4	2015 Dec 6	0000-1300
WF5	2015 Dec 8	0600-1300
WS5	2015 Dec 8-9	1300-0000
PF3	2015 Dec 10-11	2300-1200
PF4	2015 Dec 12-14	2200-0000
PF5	2015 Dec 19-20	0000-0000
WF6*	2016 Jan 21	0400-1300
WS6*	2016 Jan 21-22	1300-0700
PF6*	2016 Jan 22-24	1600-0000

Table 2.1: Frontal periods during OLYMPEX identified for use in this study. The periods are labelled by warm-frontal (WF), warm-sector (WS), post-frontal (PF) and a number to denote the order of occurrence within each frontal class. Note that all WF and WS periods are consecutive. During periods marked *, radiosonde data from the NPOL site was not available and data from the Quillayute site (UIL) was used instead (see Figure 2.1).

2.3 Measurements of precipitation

2.3.1 Rain gauges

Each OLYMPEX gauge site consists of two tipping bucket rain gauges (amongst other instruments) that were closely monitored during the field campaign. Each gauge records the exact time that enough precipitation is collected (0.254mm) to swing the tipping bucket. Data from each site was omitted if either one of the gauges was reporting an error. Otherwise, the larger of the two hourly accumulation measurements was chosen to represent each site, because tipping bucket gauges tend to underestimate precipitation (Molini et al., 2005). The data from the ‘Other gauges’ and ‘SNOTEL’ sites shown in Figure 2.1 was retrieved from Mesowest (<http://mesowest.utah.edu/>). As a quality control measure, if a gauge measures zero precipitation for an hour period whilst more than one closely neighbouring gauge (within 6km) measures more than 0.5mm, we omitted

the gauge that measures zero precipitation.

Whilst there is a high concentration of gauges in some parts of the domain, especially in the Puget Sound area, there are large areas over the Olympics (the main focus of this study) with very few gauges. The OLYMPEX gauges are concentrated along the Quinault valley area (see ‘QV’ in Figure 2.1) and therefore they are likely receive considerably less precipitation relative to the adjacent ridges (Anders et al., 2007). There is a large area on the western slopes of the Olympics (see the area labelled WS in 2.1), where there is just one gauge, in a valley. There are also no gauges over the Pacific ocean, the Strait of Juan de Fuca or the the Strait of Georgia, which further emphasises the need for remote measurements to cover these areas.

2.3.2 Radar

The two WSR-88D S-band doppler radars shown in Figure 2.1 are part of the Next-Generation Radar network (NEXRAD). Data from these radars is available from the National Centers for Environmental Information (<https://www.ncdc.noaa.gov>). Each radar performs a scanning routine approximately every 5 minutes. Each scanning routine consists of several PPI scans at several fixed elevation angles, ranging from roughly 0.5° to 5° . Each PPI scan consists of 1° wide beams transmitted every 0.5° or 1° over the full 360° of coverage. Each beam is split into 1km range bins extending from 2km to 275km away from the radar.

The following equations describe the geometry of each radar beam (Doviak and Zrnić, 1993),

$$s = k_e a \sin^{-1} \left(\frac{r \cos \alpha_e}{k_e a + h} \right) \quad \text{and} \quad (2.1)$$

$$h = (r^2 + (k_e a)^2 + 2r k_e a \sin \alpha_e)^{\frac{1}{2}} - k_e a, \quad (2.2)$$

where s is the range of the beam along the Earth’s surface from the radar, $k_e = 4/3$, a is the Earth’s radius, h is the altitude of the beam relative to the radar, r is the range of the radar beam and α_e is the elevation angle of the radar. $k_e a$ is the effective radius of the Earth, which takes into account refraction of the radar beam relative to the curvature of

the earth.

High resolution (approximately 90m) terrain data in the local area, obtained from the Shuttle Radar Topography Mission (Jarvis et al., 2008), is used to calculate partial blockage of a radar beam. Starting with the closest range bin to the radar and then moving outwards, the height of the underlying terrain is converted to the equivalent elevation angle that would intersect with the terrain, α_e^* (using (2.1) and (2.2)). The energy of the radar beam assumed to have a normal distribution with one degree beam width at half power. If

$$\alpha_e - 0.5 < \alpha_e^* < \alpha_e + 0.5 \quad (2.3)$$

then the occultation of the beam (the fraction of the beam that is blocked by the terrain) is estimated using the cumulative distribution function

$$BLK = \frac{1}{\sigma\sqrt{2\pi}} \int_{-\infty}^{\alpha_e^*} \exp\left(\frac{-(\alpha - \alpha_e)}{2\sigma^2}\right) d\alpha \quad (2.4)$$

where BLK is the occultation and $\sigma = 1/2.355$ (given the one degree beam width at half power). If $BLK > 80\%$ then the beam is assumed to be fully blocked by the terrain. Otherwise, the reflectivity (if nonzero) can be adjusted using,

$$adj = 10 \log_{10} \left(\frac{1}{1 - BLK} \right) \quad (2.5)$$

such that $dBZ_{new} = dBZ + adj$, where the subscript *new* refers to the value of reflectivity that has been adjusted for partial blockage. Therefore, if the beam is 50% blocked this corresponds to a correction of approximately +3dBZ. The amount of the beam that is blocked by the terrain is cumulative as the range increases from the radar. This process is repeated for each azimuth of a full PPI scan of the lowest two elevation angles of each radar. The results of this process for the lowest elevation angle of each radar are shown in Figure 2.5.

The adjusted data is interpolated to a common domain with 149 grid points in the x and y direction (i.e. $N_x = N_y = 149$) of size $\Delta x = \Delta y = 2\text{km}$ such that the domain is 298km^2 (this domain is used henceforth in this chapter) and then converted to an estimate of precipitation. At each grid point in the domain, the measurement from the lowest

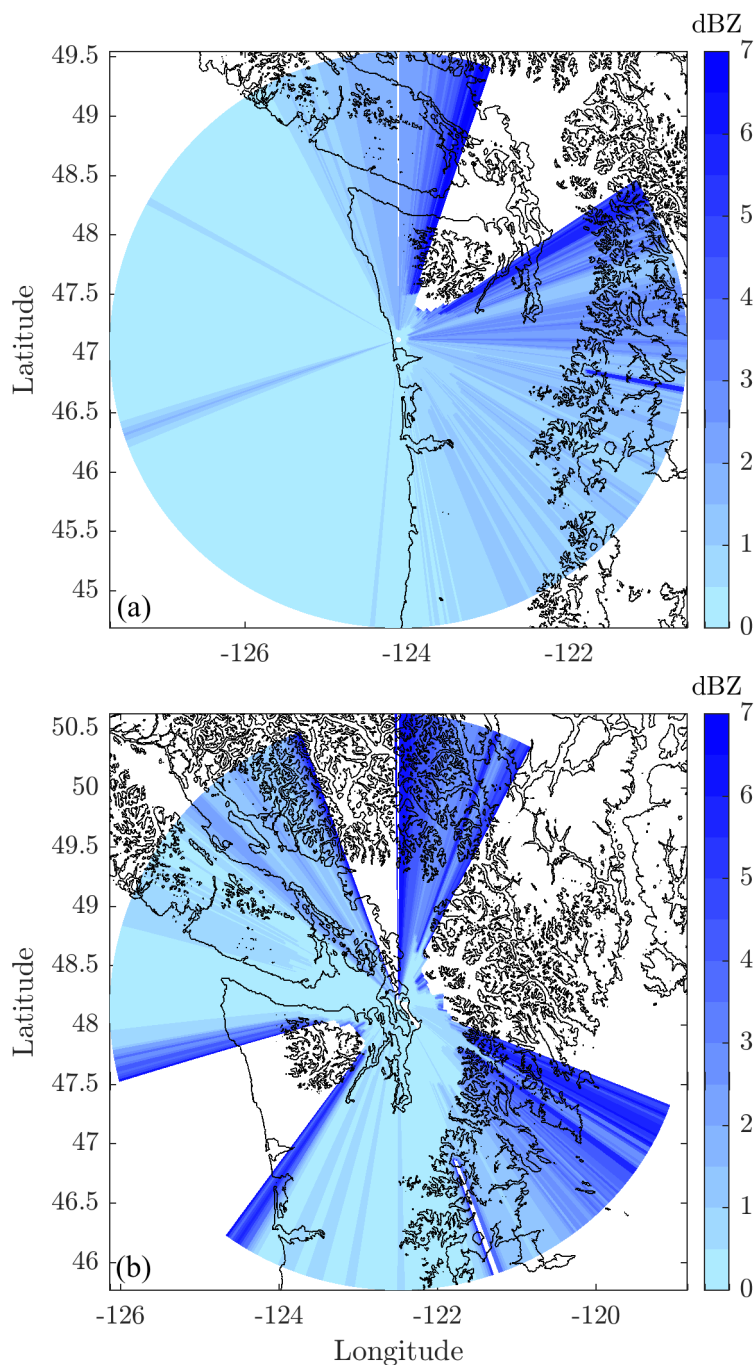


Figure 2.5: Correction added to radar data at each azimuth and range bin of the lowest elevation angle (0.5°) PPI scan for (a) the Camano and (b) the Langley Hill WSR-88D radars, due to partial blockage by terrain.

unblocked radar beam is used, as shown in Figure 2.6. The reflectivity (Z) is converted to an instantaneous precipitation rate (R) using $R = 0.028Z^{0.62}$ (the Oregon relation derived in Smith and Krajewski (1993)) and R is converted to an estimate of precipitation for each scan. This Z - R relation was chosen because the estimates of precipitation matched more closely with the gauge data in comparison to several other relations that were tested.

The resulting estimate of precipitation accumulation for the third warm-frontal period,

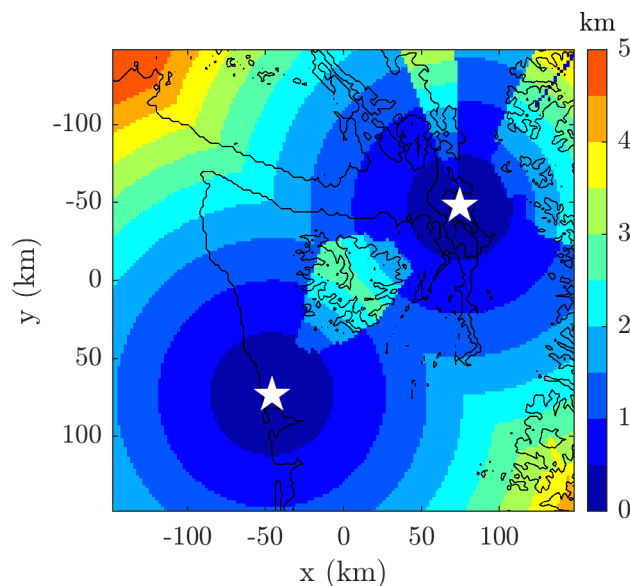


Figure 2.6: The height of the lowest unblocked radar beam interpolated to a common grid over the Olympics. The jumps in height are due to the lowest elevation angle being blocked by terrain and the next elevation angle being used. The stars indicate the location of the radars. The x and y axes indicate the distance, in km, away from a central point in the Olympics. These axes are used henceforth.

WF3 (see Table 2.1 for the time period of this event), is shown in Figure 2.7, alongside the rain gauge measurements for the same period. The spatial coverage from the radar is an improvement over the gauge network for estimating the distribution of precipitation. However, there is a large area in the middle of the Olympics in Figure 2.7(a) where there is a local minimum in precipitation, which is likely to be unphysical and yet is persistent over most of the periods outlined in Table 2.1. The rain gauge measurements in Figure 2.7(b) do not agree well with the radar derived estimate of precipitation over this area and we initially place higher confidence in the rain gauge measurements because they directly measure the accumulation of precipitation. The hourly root mean square deviation (RMSD) between all of the gauge measurements in our domain (shown in Figure 2.1) and the radar derived estimate of precipitation at the same locations is 1.19mmh^{-1} over all of the periods outlined in Table 2.1. Given this value for the RMSD and the unphysical appearance of the radar estimate field, we will merge the radar and rain gauge data to obtain an improved estimate of precipitation over the Olympics.

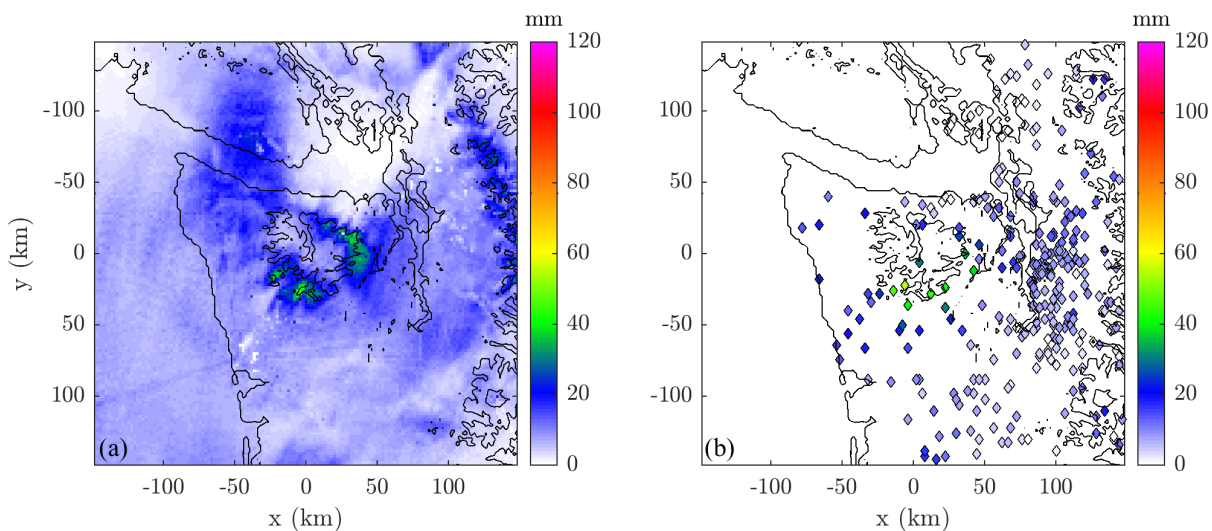


Figure 2.7: (a) Radar estimate of precipitation accumulation on the 3rd of December from 0600 to 1200 UTC (WF3) and (b) gauge measurements for the same period.

2.4 Radar and rain gauge merging

The challenge of merging radar and rain gauge data is to retain the spatial resolution of the radar data and minimize the impact of errors present in both sets of data. The RMSD between the radar and rain gauge data suggests that there are various errors in the radar estimate field. Larger-scale errors could be caused by radar miscalibration, an erroneous Z - R relation and VPR related errors (e.g., underestimating precipitation above the bright band). Smaller-scale errors may be caused by horizontal variations in the microstructure of the precipitation (especially over terrain), partial blockage and echoes from non-meteorological targets such as birds and insects. With these sources of errors in mind, a two part radar and rain gauge merging technique has been developed. Firstly, to account for the large scale errors, Mean Field Bias (MFB) correction is applied to different sections of the domain. Secondly, to account for smaller scale errors, a variational approach is used.

2.4.1 Mean field bias correction

A correction factor in an area, A , with n gauges is defined as

$$C_{MFB}(t) = \frac{\sum_{i=1}^n g_i(t)}{\sum_{i=1}^n r_i(t)} \quad (2.6)$$

where g_i is the gauge measurement at location i , r_i is the radar estimate of precipitation at the same location and t is the time that the measurements were taken. To minimize the effect of anomalous values in the radar field, r_i is taken as the mean of the 5 points closest to g_i . The entire radar estimate field within A is then multiplied by the correction factor, $R_{MFB}(t) = R(t)C_{MFB}(t)$.

Correction factors are calculated separately in areas of the domain where different radars and elevation angles are being used to estimate the precipitation, as shown in Figure 2.8. Where the beam from the lowest elevation angle from either radar is blocked over the Olympics or over the Cascades, the second-lowest elevation angle is used to estimate the precipitation in that area. This change of elevation angle can be seen in Figure 2.6 as a horizontal discontinuity where the beam height changes by approximately 1km. In stratiform precipitation, the radar reflectivity varies greatly around the freezing level due to the VPR (see Figure 1.6), and therefore we treat these areas separately. The justification for splitting the areas of the domain according to the radar being used is to account for radar miscalibration. Additionally, the area in the middle of the Olympics is treated separately (see the UPPER area labelled in Figure 2.8), because the radars are generally measuring at heights well above the freezing level (above 2500m) and because of beam broadening effects (Berenguer and Zawadzki, 2008). Both of these factors lead to an underestimation of precipitation, consistent with the local minimum seen in Figure 2.7(a). The results of MFB correction, for the same period as in 2.7, are shown in Figure 2.9.

The MFB correction adjusts the radar estimate field so that it appears more similar to the estimated climatological mean distribution of precipitation (e.g., Figure 1.1(b) or Anders et al. (2007)). However, the mean hourly RMSD between all the the gauge

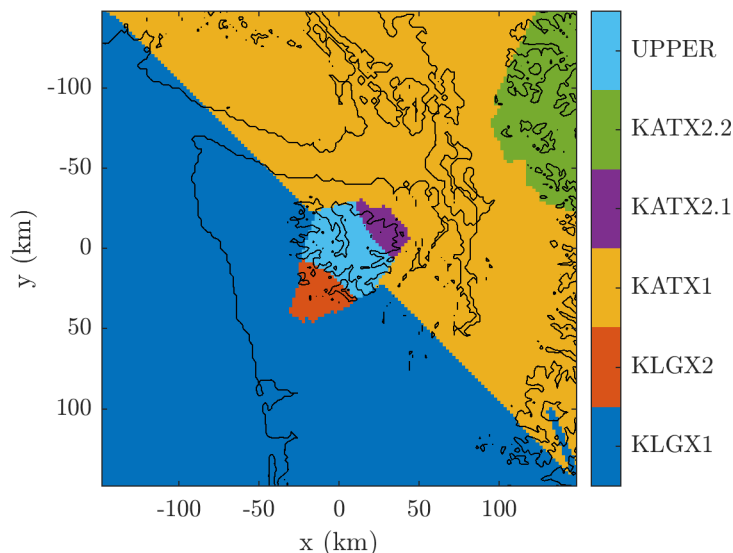


Figure 2.8: Areas of the domain in which MFB correction factors are calculated. KLGX1 and KLGX2 refer to the area of the domain covered by lowest and the second lowest elevation angle PPI scan of the KLGX radar labelled in Figure 2.1. KATX1, KATX2.1 and KATX2.2 refer to the area of the domain covered by lowest and the second lowest elevation angle PPI scan of the KATX radar labelled in 2.1. UPPER is an additional area in the middle of the Olympics that is treated separately, covered by both KLGX and KATX radars.

measurements in the domain and the MFB corrected estimate of precipitation for all the periods in Table 2.1 is not significantly reduced (from 1.19mmh^{-1} to 1.17mmh^{-1}). This may be due to the presence of smaller scale errors in the radar estimate field, such as variations in the microstructure of precipitation and partial blockage effects, which cannot be fixed by MFB correction. Therefore, we implement a variational method to improve our estimates of precipitation.

2.4.2 Variational adjustment

While the MFB method corrects some of the more prominent larger-scale errors over the high terrain, additional improvements are possible in close proximity to each gauge measurement. The 2D variational method (2DVAR) is appealing because it adjusts the radar derived precipitation estimate in close proximity to each gauge whilst also taking into account possible errors in the gauge measurements. The method outlined herein is based on optimal estimation theory and is adapted from Bianchi et al. (2013).

Define \mathbf{x} as the state vector of size S_x , in this case the 2D distribution of precipitation reduced to one dimension (e.g., if we have an 149 by 149 radar domain then $S_x =$

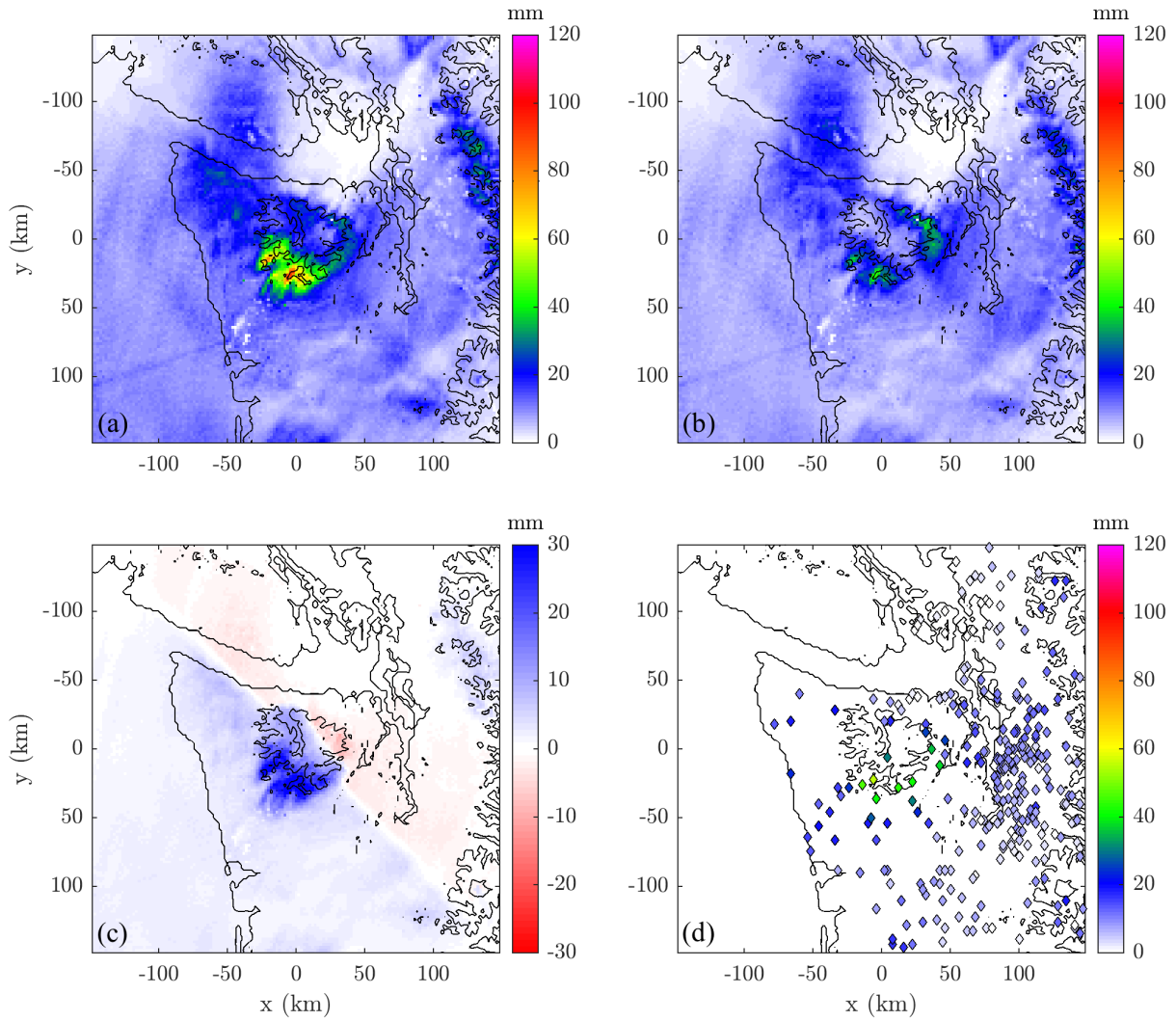


Figure 2.9: (a) Estimate of precipitation following MFB adjustment, (b) estimate of precipitation before MFB adjustment, (c) the difference between (a) and (b), (d) rain gauge measurements, for the WF3 period described in table 2.1.

149²). Define \mathbf{y} as the vector of S_y observations, in this case the number of rain gauge measurements. Then \mathbf{x} and \mathbf{y} are related by

$$\mathbf{x} = \mathbf{x}_b + \boldsymbol{\epsilon} \quad \text{and} \quad \mathbf{y} = h(\mathbf{x}) + \boldsymbol{\eta} \quad (2.7)$$

where \mathbf{x}_b is the priori estimate of the state vector (the radar estimate field), h is the nonlinear forward model that is used to compare the state vector with observations, $\boldsymbol{\epsilon}$ is the priori error and $\boldsymbol{\eta}$ is the observation error. Maximising the probability of \mathbf{x} given \mathbf{y} (as is desired), is equivalent to minimising the cost function

$$J(\mathbf{x}) = (\mathbf{x} - \mathbf{x}_b)^T \mathbf{B}^{-1} (\mathbf{x} - \mathbf{x}_b) + (\mathbf{y} - h(\mathbf{x}))^T \mathbf{R}^{-1} (\mathbf{y} - h(\mathbf{x})) \quad (2.8)$$

where \mathbf{B} and \mathbf{R} are error covariance matrices that relate to ϵ and η respectively, and $(*)^T$ denotes the transpose of the matrix $(*)$. Lower (higher) values in \mathbf{R} than in \mathbf{B} put more (less) confidence in the observations than the priori estimate. A Gauss-Newton method is used to linearise the cost function (2.8) and minimise it using an iterative equation that converges to the optimal value of \mathbf{x} .

The values in \mathbf{B} and \mathbf{R} are central to the 2DVAR method. The observation (gauge measurement) error, is assumed not to be spatially correlated, whilst the priori (radar estimate) error is assumed to be spatially correlated. In contrast to Bianchi et al. (2013), who place a higher confidence in the priori estimate when gauge measurements are more than 1.7mmh^{-1} , here the values in \mathbf{R} are fixed. \mathbf{R} is a $S_y \times S_y$ diagonal matrix with entries $R_{ii} = 0.34^2(\text{mmh}^{-1})^2$ (as in Bianchi et al. (2013) for gauge measurements less than 1.7mmh^{-1}). \mathbf{B} is a $S_x \times S_x$ matrix with values given by

$$\mathbf{B}_{ij} = \mathbf{B}_{ii} \exp\left(-\frac{d_{ij}}{d_0}\right), \quad (2.9)$$

with $\mathbf{B}_{ii} = 0.68$ (the logarithm of the radar error, obtained from Bianchi et al. (2013)), d_{ij} is the distance between the i th and j th element of the priori vector (the distance between two grid points in the domain) and d_0 is the spatial decorrelation distance, which is chosen to be 5km.

The final step of our precipitation retrieval method, which we will refer to henceforth as MFB-2DVAR, is to correct errors on larger-scales first (using MFB correction) and smaller-scales second (using 2DVAR adjustment) once per hour. The results from the 2DVAR adjustment (after MFB adjustment has already been applied) for the WF3 period is shown in Figure 2.10.

2.4.3 Verification of MFB-2DVAR method

The mean hourly RMSD between all the gauges in our domain and the radar estimate of precipitation following MFB-2DVAR adjustment for all the periods in Table 2.1 has been reduced from 1.19mm to 0.71mm, but this improvement is to be expected given that both the MFB and 2DVAR adjustment methods are designed to reduce the deviations between the radar estimate and the gauge measurements. We seek to verify the MFB-

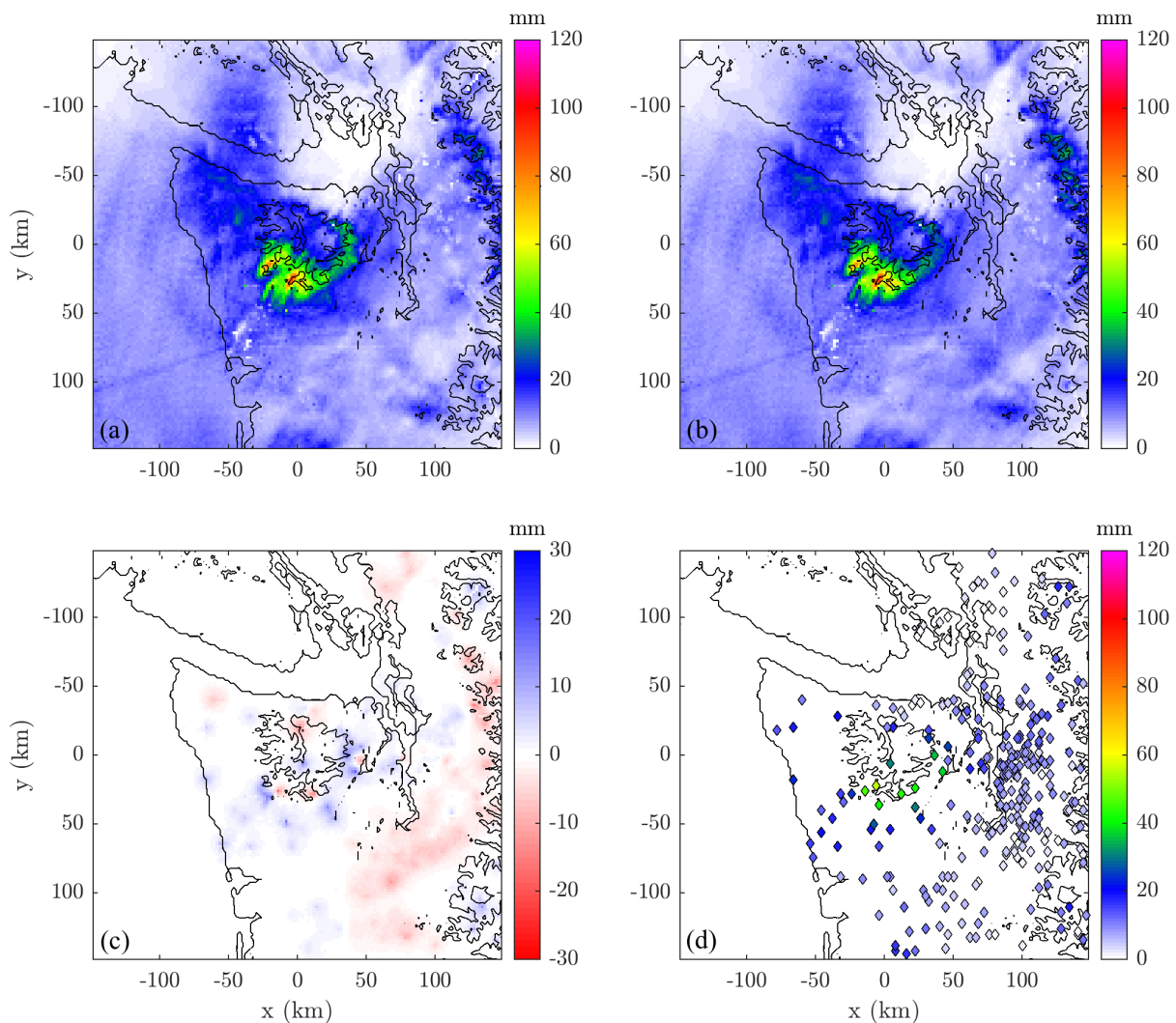


Figure 2.10: (a) Estimate of precipitation following 2DVAR adjustment, (b) estimate of precipitation before 2DVAR adjustment, (c) the difference between (a) and (b), (d) rain gauge measurements, for the WF3 period described in table 2.1.

2DVAR method further by comparing with another precipitation product.

Stage IV is a precipitation product from the National Centers for Environmental Prediction (NCEP) that merges radar data from the NEXRAD and regional rain gauge networks (Lin and Mitchell, 2005). Much like the methods used in this paper, Stage IV uses bias correction techniques together with an optimal estimation approach, but these techniques are based largely on operational experience and are more complicated than those outlined in Sections 2.4.1 and 2.4.2. Mean field bias correction is recursively estimated in each radar domain (Seo et al., 1999) and then possibly locally estimated in gauge rich areas (Fulton and Kondragunta, 2002). The optimal estimation approach outlined by Seo (1998) takes into account the fractional coverage of rainfall within an area and uses spatial correlation coefficients of radar and rain gauge data obtained from

long term climatological records of collocated measurements. Despite these more complicated and refined techniques, Stage IV was not used for the precipitation analysis in this study. This is mainly because the Stage IV analysis does not consider gauge data from OLYMPEX and it is only available (in the region and time periods of interest) every 6 hours, which is not frequent enough to bound all of the frontal periods outlined in Table 2.1. Furthermore, the spatial resolution is more larger than for our domain (4km as opposed to 2km). Nevertheless, the Stage IV product is still useful to compare with the MFB-2DVAR method.

Given the 6 hour temporal resolution of the Stage IV analysis, we cannot compare the MFB-2DVAR and Stage IV analysis over all the frontal periods in Table 2.1 and instead we have compared 6 hour intervals within three warm-frontal, warm-sector and post-frontal periods. The analyses are compared using the normalised RMSD (NRMSD) as defined by Surcel et al. (2014),

$$\text{NRMSD} = \sqrt{\frac{\sum_{x=1}^{N_x} \sum_{y=1}^{N_y} (R_1(x, y) - R_2(x, y))^2}{\sum_{x=1}^{N_x} \sum_{y=1}^{N_y} (R_1(x, y) + R_2(x, y))^2}} \quad (2.10)$$

where R_1 and R_2 are the two precipitation fields to compare (in our case the MFB-2DVAR and Stage IV estimates), N_x and N_y are the dimensions of the domain. Note that the two fields are required to have the same dimensions and resolution for this calculation and hence the Stage IV data is interpolated to the same grid that was used for the MFB-2DVAR analysis ($N_x = N_y = 149$, $\Delta x = \Delta y = 2\text{km}$). The NRMSD varies between 0 and 1, with 0 meaning that the two fields are perfectly matched and 1 meaning that the two fields are completely mismatched.

As shown in Table 2.2, the NRMSD between the MFB-2DVAR and Stage IV analysis for nine 6-hour periods varies between 0.23 and 0.52, with lower scores (better agreement between the two fields) during warm-frontal and warm-sector periods than for post-frontal periods. A comparison between the Stage IV analysis and the MFB-2DVAR method for the WF3 time period is given in Figure 2.11. Reassuringly, the products look similar for most of the domain, except for over the Olympics and over Vancouver Island. The

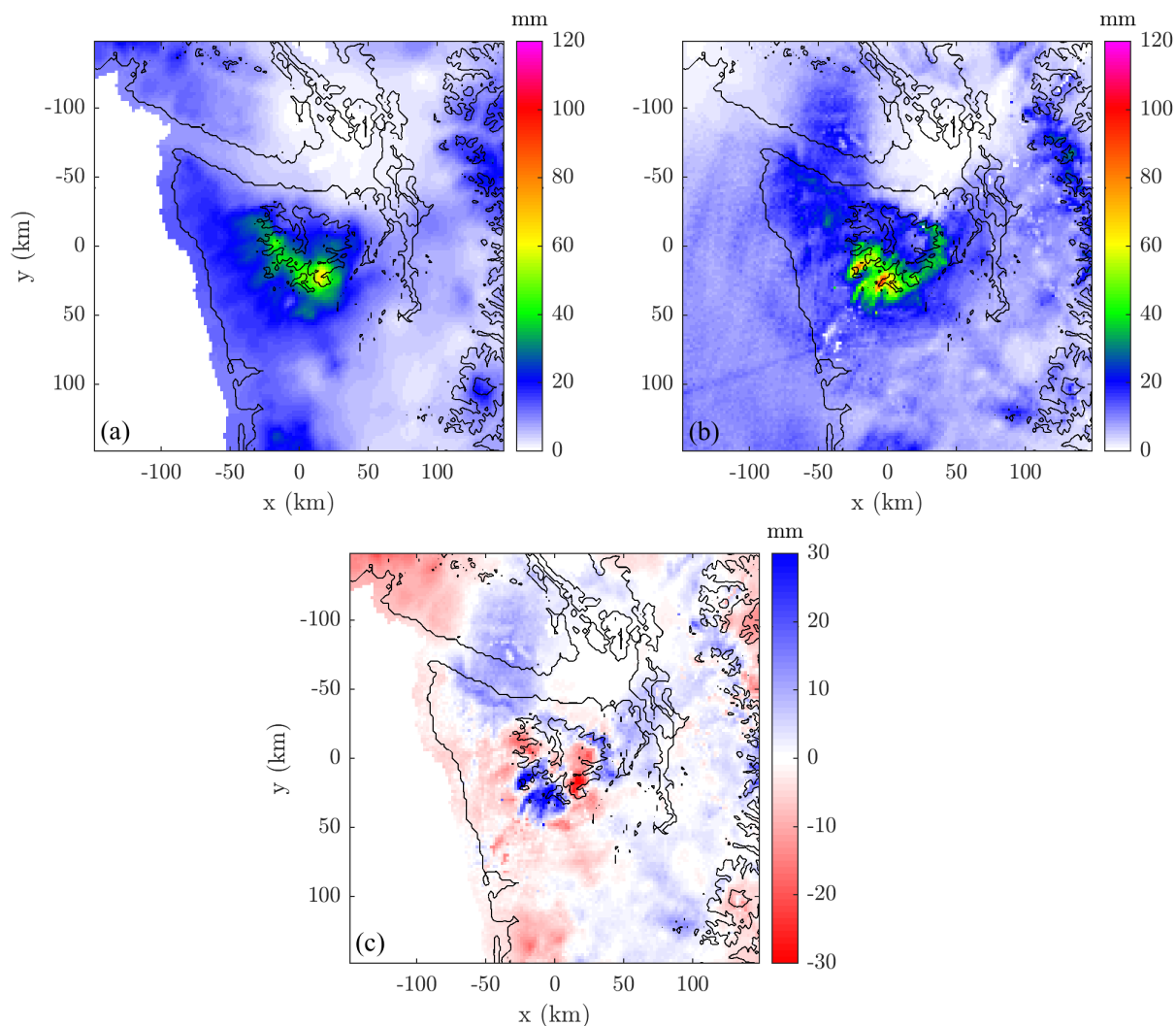


Figure 2.11: (a) Estimate of precipitation following MFB-2DVAR adjustment, (b) Stage IV estimate of precipitation, (c) the difference between (a) and (b), for the WF3 period defined in Table 2.1.

differences over the Olympics are partly due to the additional OLYMPEX gauges that are used for the MFB-2DVAR analysis. As can be seen from Figure 2.1, there are very few gauges over Vancouver Island available for this study. These gauges disagreed significantly with the radar estimates of precipitation and given that this area was not of particular focus for the study, these gauges were often omitted. Therefore, the Stage IV analysis is possibly more accurate over this area.

2.5 Results

The mean hourly precipitation rate over the Olympics using the MFB-2DVAR analysis, averaged for each of the frontal periods identified in Table 2.1 and then averaged for

Date	Time period (UTC)	NRMSD	Frontal Period
Dec 03	0600-1200	0.239	WF3
Dec 03	1200-1800	0.25	WS3
Dec 04	0600-1200	0.333	PF2
Dec 05-06	1800-0000	0.311	WF4
Dec 06	0600-1200	0.315	WS4
Dec 08	0600-1200	0.23	WF5
Dec 08-09	1800-0000	0.254	WS5
Dec 11	0000-0600	0.491	PF3
Dec 3	0000-0600	0.52	PF4

Table 2.2: NRMSD between the MFB-2DVAR and Stage IV estimates of precipitation for 6 hour periods during three warm-frontal, warm-sector and post-frontal periods in December 2015. The Frontal Period column refers to the periods from Table 2.1, in which the six hour periods are contained.

each of the frontal classes, is given in Figure 2.12. There are several key differences in the distribution of precipitation between the frontal classes. Most noticeably, the precipitation rate is significantly smaller for post-frontal periods than for the warm-frontal or warm-sector periods. Given the large scale forcing that produces precipitation ahead of a warm front and the large water vapour flux in the warm-sector, in comparison to the scattered convective precipitation observed in post-frontal conditions (as discussed in Section 1.1.1), the relatively weak precipitation rate is to be expected. All frontal classes exhibit some orographic enhancement, especially on the southwest facing slopes of the Olympics. The post-frontal periods exhibit local maxima to the south of the Olympics and at the foot of the west and southwest facing slopes of the Olympics.

The comparisons between the warm-frontal and warm-sector periods are the most compelling. Whilst there is significant orographic enhancement of precipitation in both cases, it is much greater in the warm-sector case, especially relative to the upstream precipitation (to the south west of the Olympics, over the ocean). However, there is a larger area upstream of the Olympics where the precipitation rate is enhanced for the warm-frontal periods.

2.5.1 Quantitative diagnostics

In order to quantitatively assess the differences between the frontal classes, radiosonde data from the stations shown in Figure 2.1 is used in conjunction with precipitation

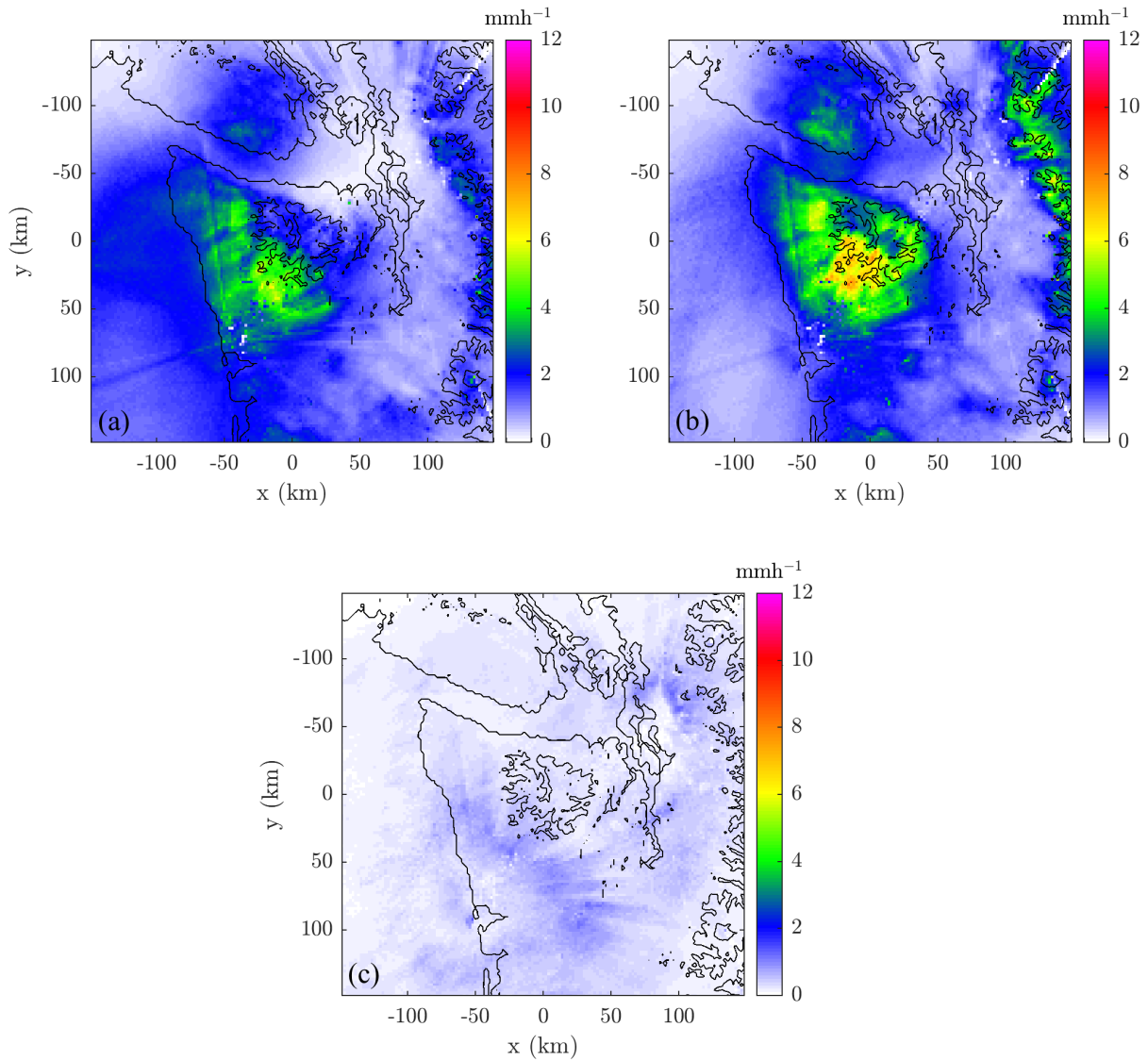


Figure 2.12: Mean distribution of hourly precipitation rate following the MFB-2DVAR method for (a) warm-frontal, (b) warm-sector and (c) postfrontal periods during OLYMPEX. The distributions are the mean of the hourly precipitation rate for the six periods of each of the frontal classes shown in Table 2.1.

distribution data (e.g., Figure 2.12). The radiosondes used for each frontal period are shown in Table 2.3. For periods where there is more than one radiosonde, the properties are calculated for each radiosonde and then the mean value is used.

To quantify the mean properties of the impinging flow, the mean cross-barrier wind speed (\bar{U}), the moisture flux (I), the upstream precipitation rate (R_{up}) and the nondimensional mountain height (ϵ) are used. To quantify the response of the flow to the mountain we use the absolute orographic enhancement (AE) and the drying ratio (DR).

Given that the Olympics is a quasi-circular barrier, there is no fixed cross-barrier direction and we calculate the moisture-flux weighted wind direction for each sounding

Period	Site	Date	Launch Time (UTC)
WF1	NPOL	2015 Nov 12	1805
	NPOL	2015 Nov 12	2110
WS1	NPOL	2015 Nov 13	0305
	NPOL	2015 Nov 13	0610
	NPOL	2015 Nov 13	0928
WF2	NPOL	2015 Nov 17	0812
WS2	NPOL	2015 Nov 17	1115
	NPOL	2015 Nov 17	1502
PF1	NPOL	2015 Nov 18	0213
	NPOL	2015 Nov 18	0515
	NPOL	2015 Nov 18	1725
	NPOL	2015 Nov 18	2315
WF3	NPOL	2015 Dec 03	0712
WS3	NPOL	2015 Dec 03	1516
	NPOL	2015 Dec 03	1915
PF2	NPOL	2015 Dec 04	0514
	NPOL	2015 Dec 04	1517
	NPOL	2015 Dec 04	1719
WF4	NPOL	2015 Dec 05	1514
	NPOL	2015 Dec 05	1913
WS4	NPOL	2015 Dec 06	0517
WF5	NPOL	2015 Dec 08	0713
WS5	NPOL	2015 Dec 08	1515
	NPOL	2015 Dec 08	1915
PF3	NPOL	2015 Dec 11	0513
	NPOL	2015 Dec 11	0513
PF4	NPOL	2015 Dec 13	0724
	NPOL	2015 Dec 13	1516
	NPOL	2015 Dec 13	1916
PF5	NPOL	2015 Dec 19	0215
	NPOL	2015 Dec 19	0517
WF6	UIL	2016 Jan 21	1200
WS6	UIL	2016 Jan 22	0000
PF6	UIL	2016 Jan 22	1200

Table 2.3: Soundings used for calculating upstream flow properties for the periods outlined in Table 2.1. The locations of the sites NPOL and UIL are marked on Figure 2.1.

instead. Firstly, we define the total moisture flux I_{tot} ,

$$I_{tot} = \int_{p_1}^{p_2} -\frac{1}{g} U_{tot} q_v dp, \quad (2.11)$$

where p is the atmospheric pressure, g is the gravitational acceleration, U_{tot} is the wind speed, q_v is the water vapour mixing ratio, $p = p_1$ and $p = p_2$ are the upper and lower

boundaries of the individual sounding respectively. Then the cross-barrier wind direction is taken to be the average of the wind direction weighted by I_{tot} at each vertical level. Similarly, the mean cross-barrier wind speed is defined by

$$\bar{U} = \frac{\int_{p_{sfc}}^{p_h} U_{cb} I dp}{\int_{p_{sfc}}^{p_h} I dp} \quad (2.12)$$

where $h = 2432\text{m}$ is the peak of Mount Olympus (NGS, 1990), p_{sfc} and p_h is the pressure at the surface and at h respectively, and U_{cb} is the component of U_{tot} that is parallel to the moisture-flux weighted (cross-barrier) wind direction. I is defined using (2.11) except that U_{tot} is replaced with U_{cb} and we integrate from the surface to the top of the sounding.

For the nondimensional mountain height, $\epsilon = Nh/\bar{U}$, the Brunt-Väisälä frequency is obtained following the average stability estimate method outlined in Reinecke and Durran (2008),

$$N = \frac{1}{h} \int_0^h N(z) dz \quad (2.13)$$

where $N(z)$ is calculated following Durran and Klemp (1983). If the relative humidity is greater than 0.98 then we use the moist Brunt-Väisälä frequency, $N = N_m$, and

$$N_m^2 = \frac{g}{T} \left(\frac{dT}{dz} + \Gamma_m \right) \left(1 + \frac{Lq_s}{RT} \right) - \frac{g}{1+q_v} \frac{dq_v}{dz} \quad (2.14)$$

where T is the temperature, L is the latent heat of vaporization, q_s is the saturated water vapour mixing ratio, R is the ideal gas constant for dry air and Γ_m is the moist adiabatic lapse rate. If the relative humidity is less than 0.98 then N is the dry Brunt-Väisälä frequency, $N = N_d$, and

$$N_d^2 = g \frac{d \ln \theta}{dz} \quad (2.15)$$

where θ is the potential temperature.

DR is defined by Smith et al. (2003) as $DR = P/I$ where P is the precipitation that falls out over the mountain. To calculate P , we need a one dimensional (1D) precipitation rate. Hence for a given precipitation distribution (from our analysis in the previous section) we take a 40km wide transect centered over the Olympics, across the whole of

our domain, parallel to the cross-barrier wind direction, and take the mean precipitation over the width of this transect to reduce it to a 1D precipitation rate. The length of this transect varies depending on its orientation in the domain. We define

$$P = \int_{-L}^L R(x)dx \quad (2.16)$$

where $R(x)$ is the precipitation rate at location x , $x = 0$ is a midpoint of the Olympics and L is a characteristic length scale, such that $x = -L$ is upstream of the mountain and $x = L$ is downstream of the mountain. L is obtained by taking the Fourier transform of the 1D terrain height (which is obtained the same way as the 1D precipitation rate) and converting the wavenumber with the largest amplitude to a distance. L is approximately 100km, but this value varies with the cross-barrier wind direction.

With the above definition, $DR > 0$ even if the mountain produces no enhancement in situations with large-scale precipitation (i.e. where precipitation would occur anyway over land, even if the mountain was absent). Given that we are interested in the orographic enhancement of precipitation relative to the upstream precipitation rate, we define an alternative drying ratio, $DR^* = P^*/I$, with

$$P^* = \int_{-L}^L (R(x) - R_{up})dx, \quad (2.17)$$

where R_{up} (the mean upstream precipitation rate) is the mean of the 1D precipitation rate that is greater than one characteristic length scale further upstream ($x < -L$) of the mountain (as stated earlier, the length of the 1D precipitation rate changes depending on the cross-barrier wind direction). We define AE simply as $AE = R_{max} - R_{up}$, where R_{max} is the maximum precipitation rate in a 100km^2 sub-domain centered over the Olympics.

The properties of the six warm-frontal, warm-sector and post-frontal periods from Table 2.1 are shown in Table 2.4, with the mean for each frontal class. The upstream flow parameters (\bar{U} , I , R_{up} and ϵ) fit with what would be expected given our previous discussion of the properties of soundings for each synoptic class (Section 1.1.1). \bar{U} is much smaller for post-frontal than warm-frontal and warm-sector periods, hence I is also much smaller and ϵ is considerably larger. R_{up} is largest for the warm-frontal periods

and ϵ is greater for warm-frontal than warm-sector periods, due to the stable inversion that is often present in warm-frontal soundings (note that \bar{U} is similar in warm-frontal and warm-sector cases).

	\bar{U} ms ⁻¹	I kgm ⁻¹ s ⁻¹	R_{up} mmh ⁻¹	ϵ	AE mmh ⁻¹	DR	DR^*
WF1	20	419	2.18	1.21	9.4	0.406	0.097
WF2	17	459	3.35	1.54	2.48	0.217	-0.225
WF3	25	652	1.49	1.05	13.6	0.234	0.0909
WF4	30	528	1.38	0.938	10.6	0.188	0.0443
WF5	17	450	0.841	0.835	8.57	0.26	0.14
WF6	21	643	1.96	1.17	6.85	0.224	0.0455
WF	21.7	525	1.87	1.12	8.58	0.255	0.0321
WS1	22	656	1.16	0.609	13.9	0.31	0.199
WS2	22	667	0.989	0.542	11.6	0.263	0.173
WS3	33	737	0.816	0.689	12.3	0.166	0.0961
WS4	22	451	1.15	0.66	10.2	0.197	0.0535
WS5	23	723	0.692	0.907	9.44	0.196	0.135
WS6	18	605	2.01	0.829	7.16	0.249	0.0621
WS	23.3	640	1.14	0.706	10.8	0.23	0.12
PF1	13	178	0.0826	2.37	1.04	0.0484	0.0229
PF2	7	92	0.413	3.18	1.55	0.22	-0.068
PF3	14	185	0.544	1.45	2.09	0.185	0.0109
PF4	18	209	0.331	1.17	2.61	0.244	0.145
PF5	8	94	0.0689	2.73	1.34	0.111	0.0654
PF6	8	78	0.529	3.86	0.883	0.312	-0.113
PF	11.3	139	0.328	2.46	1.59	0.187	0.0105

Table 2.4: Properties of the warm-frontal, warm-sector and post-frontal periods outlined in table 2.1 and the mean properties for each class; labelled WF, WS and PF respectively.

As expected, AE is largest for warm-sector periods and much smaller during post-frontal periods than for the other frontal classes. However, DR is relatively similar for each of the frontal classes. DR^* appears to reflect the qualitative differences between the precipitation distributions much better than DR , given that it is largest for warm-sector periods, then considerably smaller for warm-frontal periods and smaller again for post-frontal periods. The key differences between the parameters for each frontal class are seen most clearly by comparing the mean values in Table 2.4 (labelled without a number), but they are also generally reflected on a case by case basis (recall that the warm-frontal and warm-sector periods with the same number are consecutive and therefore they can be directly compared).

2.6 Discussion

We have classified six warm-frontal, warm-sector and post-frontal periods during OLYMPEX and retrieved the mean distribution of precipitation for each frontal class. Precipitation was first estimated using radar data and then adjusted with rain gauge data by using a combination of bias correction and optimal estimation techniques. Our precipitation retrieval technique significantly reduced the deviation between the radar estimate of precipitation and the rain gauges.

The mean distribution for all frontal classes exhibited an orographic enhancement of precipitation, especially on the southwest facing slopes of the Olympics, but post-frontal periods produced much less precipitation than the other classes. Warm-sector periods exhibited the largest orographic enhancement of precipitation, whilst warm-frontal periods exhibited a larger area upstream of the mountain in which precipitation was enhanced, and post-frontal periods exhibited a maximum in precipitation at the foot of the mountain. Quantitative analysis was performed on the frontal periods by using a combination of upstream radiosonde data and the retrieved precipitation distributions. Properties of the upstream flow (\bar{U} , I , R_{up} and ϵ) are compared to parameters that are used to assess the response of the flow to the mountain (AE , DR and DR^*) in Table 2.4.

The consideration of upstream precipitation makes a crucial difference to the analysis; DR is similar between the 3 frontal classes, but DR^* is much larger for warm-sector than warm-frontal and post-frontal periods. DR is the largest for warm-frontal periods, which indicates that the most precipitation is produced by the mountain during warm-frontal periods. However, it is clear by comparing Figures 2.12(a) and (b) that warm-sector periods produce the largest orographic enhancement of precipitation, which is reflected in DR^* , whilst warm-frontal periods have a larger R_{up} and exhibit a more modest orographic enhancement over a larger area upstream of the mountain, which is reflected in DR . The large DR^* suggests that warm-sector periods are more efficient at converting the incoming water vapour to precipitation than warm-frontal and post-frontal periods. Previously, others have observed a similar result, especially that warm-sector conditions produce the largest orographic enhancement of precipitation (e.g., Browning et al., 1974).

We hypothesize that ϵ greatly influences the distribution and orographic enhance-

ment of precipitation because it is correlated with the fraction of the flow that is diverted around the mountain as opposed to ascending it (e.g., Reinecke and Durran, 2008). In theory, larger ϵ means greater horizontal deflection, less ascent and hence less orographically forced clouds and precipitation. Table 2.4 supports this hypothesis because ϵ and DR^* appear to be inversely correlated. There is also a significant upstream shift in the enhancement of precipitation for the warm-frontal periods (Figure 2.12(a)) compared to the warm-sector periods (Figure 2.12(b)). This indicates that more of the flow is blocked because the flow stagnates as it approaches the mountain (see Figure 1.5), which is reconciled by the relatively large ϵ for warm-frontal periods. These results support the findings of Houze et al. (2001), who observed that blocked flow (larger ϵ) produced an upstream shift in the enhancement of precipitation and a decreased enhancement of precipitation over the Mediterranean side of the Alps in comparison to unblocked flow (smaller ϵ).

Only six periods for each frontal class are included because this is the maximum number of warm-frontal periods during OLYMPEX that were easily classifiable following the methods outlined in Section 2.2. Outside of the OLYMPEX period, the number of gauges in the Olympics is significantly reduced (especially on the windward slopes) and radiosonde data is only available from the Quillayute station (UIL) in 12-hourly intervals. Both of these factors would negatively influence the reliability of our precipitation analysis. We acknowledge that six events are not enough to produce a climatology of frontal periods and therefore we support the results from this chapter in the next chapter, by using numerical simulations as an additional data source.

Chapter 3

Modelling

3.1 Introduction

In this chapter, quasi-idealized simulations of frontal periods over the Olympics terrain will be outlined. Preliminary results from the simulations are presented and verified against the observational precipitation analysis from Chapter 2.

As opposed to using the observed soundings to initialize simulations, we use idealized soundings that are based on the observed soundings. Using this approach, the characteristics of the upstream flow conditions for each frontal period can be isolated and systematically analyzed. For example, the warm-frontal and warm-sector soundings are constructed such that they differ primarily by the presence of a stable inversion in the lower atmosphere. In order to avoid the complex temporal variability in the atmospheric profile associated with the passing of an extratropical cyclone, each frontal period is characterized by either a single quasi-steady flow (for warm-sector) or the mean of several quasi-steady flows (for warm-frontal and post-frontal).

A key innovation of the simulations herein is the consideration of non-orographic precipitation processes. As discussed in Section 1.2.3, the presence of upstream precipitation has been largely neglected in idealized simulations of orographic precipitation. We address this issue in two ways. Firstly, for the warm-frontal and warm-sector periods, a horizontally uniform vertical lifting profile is applied over the domain to produce stratiform precipitation. Here we have made a simplification that the ascent during warm-frontal periods is vertical as opposed to slantwise, which allows us to use the same framework

to produce upstream precipitation in both cases. Secondly, oceanic cellular convection is produced upstream of the Olympics to mimic convective precipitation during post-frontal periods. Surface fluxes from the ocean to the atmosphere are balanced by horizontally uniform cool air advection to produce moist instability and random potential temperature perturbations are used to trigger convection.

This chapter will be limited to the presentation of the results from simulations, comparison with the results from Chapter 2 and additional sensitivity tests of the upstream precipitation rate. In-depth analysis of the simulations is ongoing work that will not be presented in this thesis.

3.2 Numerical setup

3.2.1 General

Numerical simulations are conducted using the Weather Research and Forecasting model (WRF) Version 3.7, which is compressible, non-hydrostatic and Eulerian. Lateral boundary conditions are periodic in x and y and hence the domain size is chosen to be large enough such that perturbations do not circulate the domain within the run time for each simulation. We use a 960km by 480km domain in the x and y direction respectively, with equal grid spacing of $\Delta x = \Delta y = 2\text{km}$, hence 480 by 240 grid points. There are 100 vertical levels that are evenly spaced in hydrostatic pressure from the surface up to 20 km, with rigid boundary conditions on the top. There is a gravity wave damping layer in the top 8km of the domain to reduce reflections of gravity waves. A third order Runge-Kutta scheme is used to integrate in time and advection is fifth order in the horizontal and third order in the vertical.

To focus on the pure impacts of the Olympics terrain on the precipitation, the USGS terrain data from Chapter 2 is truncated around the Olympics massif. It is also smoothed by a 3-point boxcar method to largely eliminate $2\Delta x$ waves that give rise to large model errors. The coastline surrounding the Olympics is also truncated ($\pm 1.5^\circ$ in latitude and $\pm 1.25^\circ$ in longitude from the midpoint of the Olympics), to avoid sharp gradients in surface type across periodic lateral boundaries. Thus, the simulations consider the

impacts of both the Olympics and the upstream (western) shoreline. The terrain height in the model domain is shown in Figure 3.1.

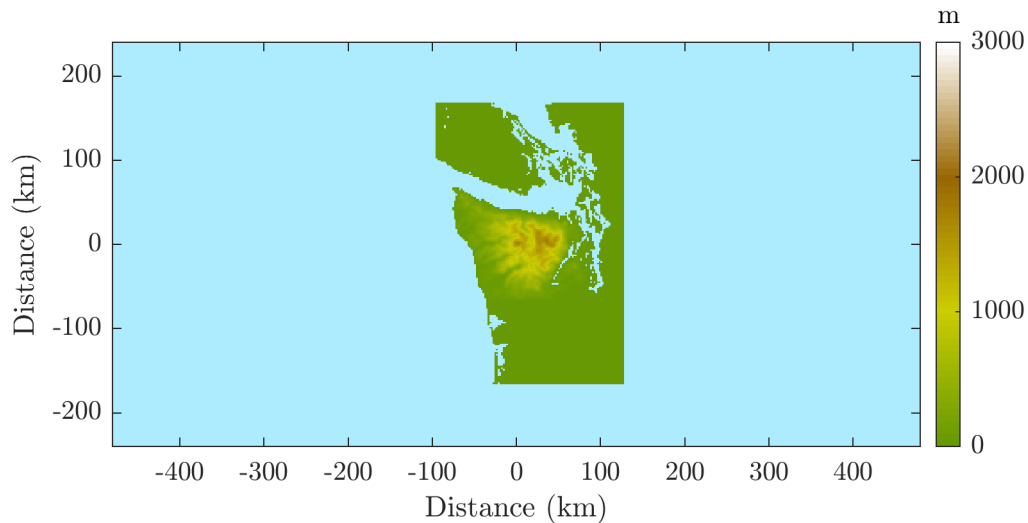


Figure 3.1: Terrain height and land use for the domain used in simulations. The blue represents the area that is treated as ocean.

The Thompson et al. (2008) bulk microphysical parametrization scheme is used and the planetary boundary layer is treated with the Yonsei University Scheme (Hong et al., 2006). The surface is parameterized by a no-slip condition with a roughness length that varies between land and water: ocean surfaces are treated as water bodies with an aerodynamic roughness length of 0.01 cm and land areas are treated as evergreen needleleaf forest with an aerodynamic roughness length of 50cm. The Coriolis force is only applied to flow perturbations from the base state. The simulations are initialized based on a single sounding, which is applied over the entire domain. Three different soundings are used for the three different frontal periods of interest (warm-frontal, warm-sector and post-frontal), based on the statistics of observed soundings during OLYMPEX (e.g., Figures 1.3 and 2.3). Particular care is applied to matching the values of I , \bar{U} , and ϵ from the observations, to evaluate the importance of each parameter on the resulting orographic precipitation.

3.2.2 Warm-frontal

Examples of observed warm-frontal soundings that the idealized warm-frontal soundings are based on are shown in Figure 1.3(a) and 2.3(a). The idealized warm-frontal soundings consist of 4 layers that vary predominantly by their Brunt-Väisälä frequency. The bottom

three of these layers have relative humidity $RH = 0.99$ and are assumed to be saturated. Starting from the surface, the temperature is set to 9°C and the bottom layer is slightly stable with $N_m^2 = 5 \times 10^{-5}\text{s}^{-2}$. The bottom layer is topped by a thin stable inversion layer, which simulates the altitude-varying frontal inversion that bounds a cooler air mass below and a warmer air mass above (a stable inversion is positioned at approximately 1.5km in Figure 1.3(a) and at the surface in Figure 2.3(a)). The frontal inversion layer has $N_m^2 = 4 \times 10^{-4}\text{s}^{-2}$ and is 400m thick. From the top of the inversion up to the tropopause, which is fixed at 12km, the atmosphere has a pseudoadiabatic profile, such that $N_m^2 = 0$. The relative humidity decreases to $RH = 0.50$ in the stratosphere, whereby the atmosphere is assumed to be unsaturated and the Brunt-Väisälä frequency increases to $N_d^2 = 4 \times 10^{-4}\text{s}^{-2}$. The wind speed increases linearly from 10ms^{-1} at the surface to 25ms^{-1} at 1.3km, then to 50ms^{-1} at 12km (the tropopause), above which it stays constant. Veering winds, consistent with warm air advection, are observed below the inversion in warm frontal soundings (e.g., below 1.5km in Figure 1.3(a)). Therefore for the idealized soundings, whilst the vertical profile of wind speed is fixed for the soundings with different inversion heights, the wind direction veers linearly from 190° to 240° between the surface and the inversion height, above which it is constant. An example idealized warm-frontal sounding with the lower boundary of the inversion layer set at $z_{inv}=2\text{km}$ is given in Figure 3.2.

During warm-frontal periods, the inversion gradually descends towards the surface as the surface warm front approaches. We avoid this complex time variability by taking the mean of three quasi-steady simulations, with $z_{inv}=3\text{km}$, 2km and 1km , to represent a warm-frontal period. An upper limit of 3km is chosen because all but one of the observed soundings from Table 2.3 exhibit an inversion within this range.

A horizontally uniform vertical lifting profile is applied over the domain to simulate the warm air mass ascending slantwise over the cooler air mass, which in turn produces precipitation. The lifting is parameterized by adding an advective term $-w_{ls}\partial\phi/\partial z$ to the tendencies for potential temperature and all water species, where $w_{ls}(z) = w_{max} \sin(\pi(z - z_b)/d)$ is the imposed lifting profile, w_{max} is the lifting amplitude, $z_b = 3.4\text{ km}$ is the base of the lifting layer (chosen because this is the top of the highest inversion), $d = z_t - z_b$,

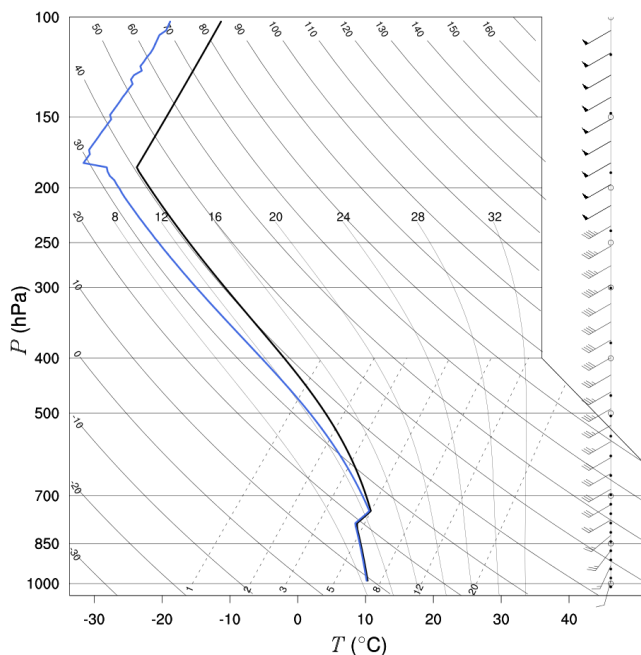


Figure 3.2: An idealized sounding used to initialize warm-frontal simulations, with $z_{inv}=2\text{km}$. The number of lines on the tails of the wind barbs represent a wind speed of 10ms^{-1} each and the solid black triangle represents 50ms^{-1} . The solid black line is the temperature profile and the blue line is the dew point temperature.

and $z_t = 12 \text{ km}$ is the tropopause height.

To ensure that the impinging flow is maintained in a quasi-steady state, surface heat fluxes are switched off. The simulations are found to reach a steady state after approximately 2 hours and therefore the mean hourly precipitation distribution is taken as the last 3 hours of a 6 hour long simulation.

3.2.3 Warm-sector

Warm-sector soundings mainly differ from warm-frontal soundings in that there is no stable inversion layer on the surface, as can be seen in the example observed warm-sector soundings in Figures 1.3(b) and 2.3(b). Therefore, the idealized warm-sector sounding is exactly the same as the warm-frontal soundings without the lowest two statically stable layers and without veering winds, as can be seen in Figure 3.3. The atmosphere follows a pseudoadiabatic profile from the surface to the tropopause and the wind direction is fixed at 240° . The equivalent potential temperature at the tropopause is held fixed between the warm-frontal and warm-sector soundings such that when this is extrapolated down to

the surface, a temperature of 12°C is obtained. The vertical profiles of relative humidity, wind speed and lifting are the same as for the warm-frontal soundings, with w_{max} varied to produce different values of upstream precipitation. The warm-sector simulations are also found to reach a steady state after approximately 2 hours and therefore the mean hourly precipitation distribution is taken as the last 3 hours of a 6 hour long simulation, the same as for the warm-frontal simulations.

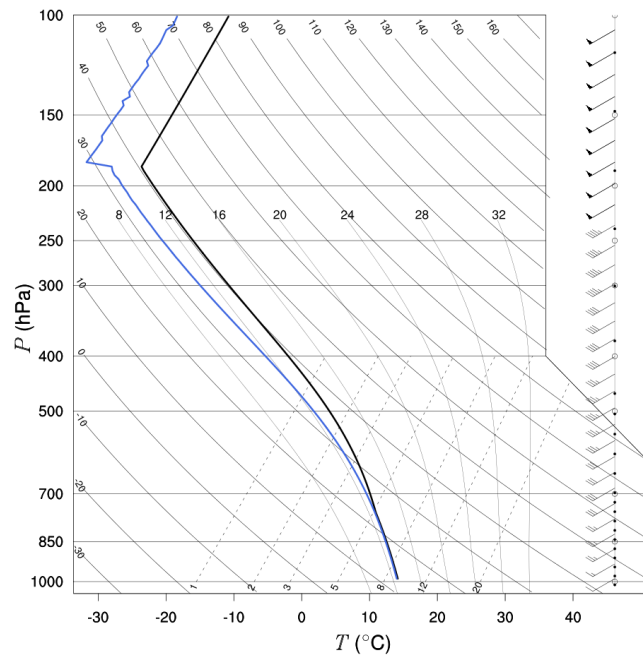


Figure 3.3: Idealized sounding used to initialize warm-sector simulations. The wind barbs and the temperature profiles are as explained in the caption of Figure 3.2.

3.2.4 Post-frontal

Observed post-frontal soundings differ quite significantly from warm-frontal and warm-sector soundings in that the atmosphere is colder, the tropopause is closer to the surface, the air is drier, there is often a conditionally unstable layer near the surface and the wind speed is significantly slower. These features can be seen in the examples of post-frontal soundings shown in Figures 1.3(c) and 2.3(c). Therefore, the idealized post-frontal sounding (Figure 3.4) consists of three layers of varying static stability. The lowest layer is slightly conditionally unstable, with $N_m^2 = -5 \times 10^{-5} \text{s}^{-2}$ and $RH = 0.9$ from the surface to 3km. From 3km to the height of the tropopause (which is now lowered to 8.5km)

the atmosphere is stable, with $N_d^2 = 1 \times 10^{-4} \text{s}^{-2}$ and the relative humidity decreases linearly from $RH = 0.9$ to 0.5, and it remains at 0.5 from the tropopause up to the top of the atmosphere (20km). The wind speed increases linearly from 5ms^{-1} at the surface to 50ms^{-1} at the tropopause and then remains constant. Whilst some observed post-frontal soundings exhibit significant backing with height (such as in Figures 1.3(c) and 2.3(c)), the majority of the observed post-frontal soundings did not and hence we use a uni-directional wind profile.

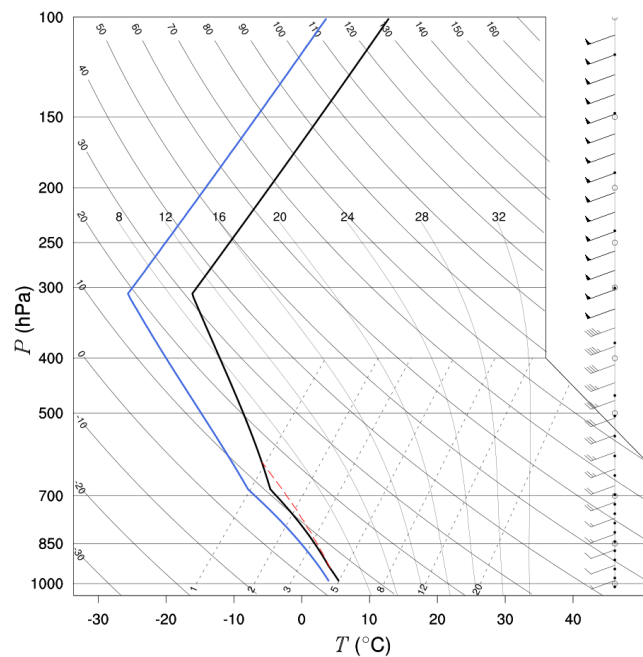


Figure 3.4: Idealized sounding used to initialize post-frontal simulations. The wind barbs and the temperature profiles are as explained in the caption of Figure 3.2.

In contrast to the warm-frontal and warm-sector simulations, there is no vertical lifting profile. However, because post-frontal flows are characterized by convection over the open ocean due to the advection of cold, dry air over the warmer ocean surface, we include surface heat fluxes and large-scale cooling. While the surface skin temperature over land is set to be equal to the surface air temperature, the initial sea-surface temperature is set 2°C higher than the surface air temperature, causing a convective mixed layer to develop over the ocean. Convection within this layer is seeded by initial random potential-temperature perturbations with a maximum amplitude of 0.1°C . Large-scale cooling in the lowest unstable layer of the atmosphere (0-3km) is at a rate of -2°C per day. The post-frontal simulations are found to take longer to reach a steady state than the warm-frontal and

Label	Type	w_{max} (ms ⁻¹)	z_{inv} (km)	Fluxes	Quantity
wf-control	warm-frontal	0.3	1, 2 and 3	no	3
wf-wm0.2	warm-frontal	0.2	1, 2 and 3	no	3
wf-wm0	warm-frontal	0	1, 2 and 3	no	3
ws-control	warm-sector	0.2	none	no	1
ws-wm0.3	warm-sector	0.3	none	no	1
ws-wm0	warm-sector	0	none	no	1
pf-control	post-frontal	-	none	yes	4
pf-noflux	post-frontal	-	none	no	4

Table 3.1: Details of the simulations discussed herein. The Fluxes entry refers to whether or not the surface fluxes and advective cooling outlined in Section 3.2.4 are being used. The Quantity entry refers to the number of simulations that are averaged for each case.

warm-sector simulations; they are run for 12 hours and the average hourly precipitation rate is obtained from the mean of the last 6 hours of the simulations. Finally, because convective precipitation tends to produce irregular precipitation patterns, we run four versions of each simulation that are identical except that they use different initial random perturbations. The different locations of cellular convection in these simulations provides some useful smoothing to provide a more meaningful comparison with observations.

3.3 Simulations

The simulations discussed herein are described in Table 3.1. The value of w_{max} is varied between the warm-frontal and warm-sector control cases (wf-control and ws-control respectively) so that the values of R_{up} match closely with the observed values. Sensitivity tests are performed where these values of w_{max} are swapped (wf-wm0.2 and ws-wm0.3), as well being set to zero (wf-wm0 and ws-wm0), to determine the significance of R_{up} on the resulting precipitation distributions.

Figures 3.5(a), (b) and (c) show the simulated surface radar reflectivity in the middle of the averaging period for each control case. The wf-control and ws-control reflectivity fields show broadly uniform precipitation in the horizontal (as expected from the horizontally uniform large-scale forcing), along with some precipitation enhancement over and upstream of the mountain and relatively weak precipitation in the rain shadow directly downstream of the mountain. As the wf-control and ws-control simulations develop, there are some cellular patterns in the reflectivity field, which can be attributed to a weak in-

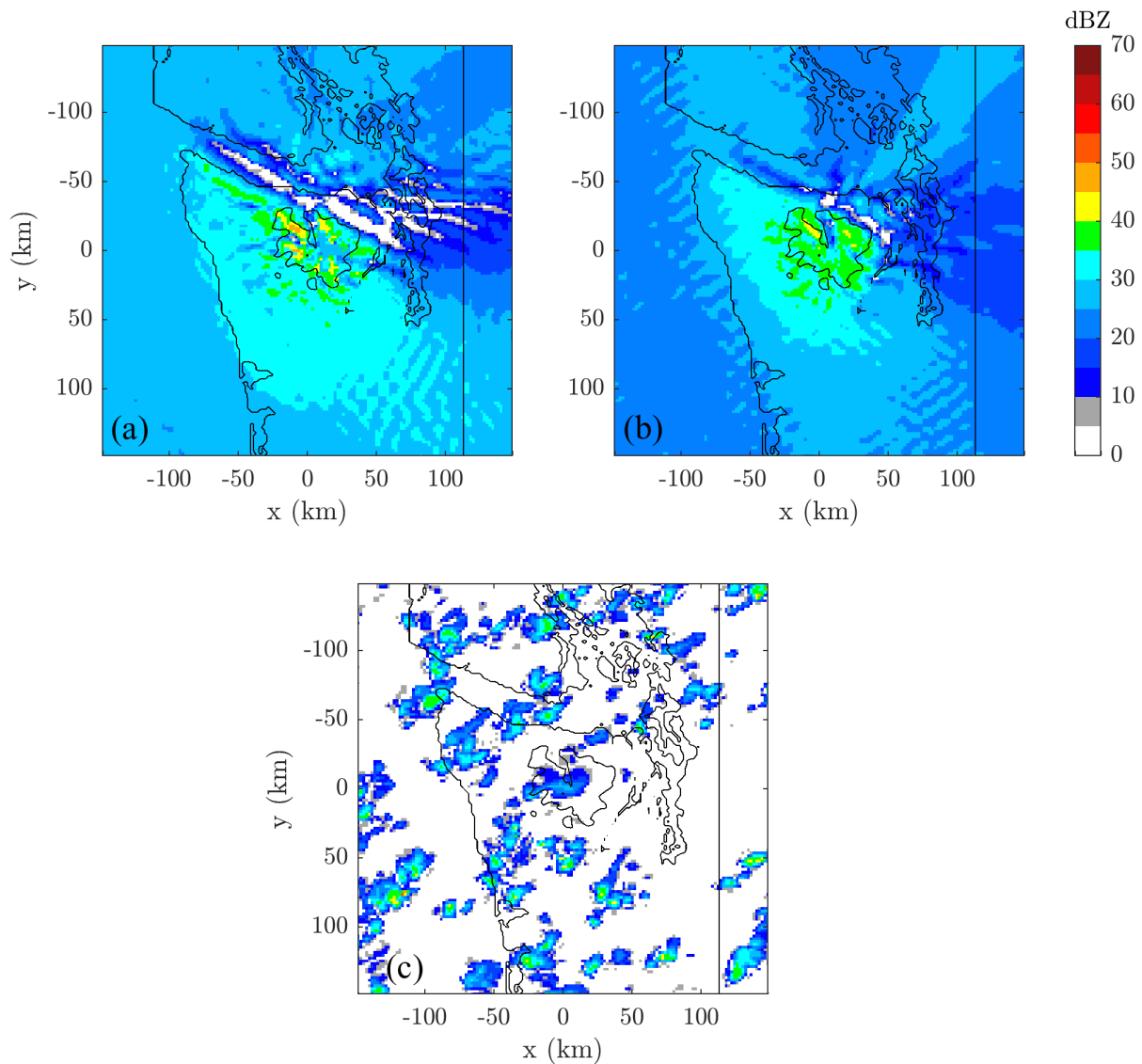


Figure 3.5: Simulated radar reflectivity for: (a) the wf-control case with $z_{inv} = 2\text{km}$ at 4.5 hours into the simulation, (b) the ws-control case at the same time into the simulation, (c) one of the pf-control simulations at 9 hours. The times are chosen because they are half way into the respective periods that are used to calculate the mean hourly precipitation distribution. Here and henceforth, the black contours in the figures from simulations show the coastline and terrain height in intervals of 1km.

stability that develops near the melting layer (e.g., Houze and Medina, 2005). Hence the simulations do not exactly reach a steady state, but the influence of these cells is minor. The reflectivity field for the post-frontal control simulation (pf-control) shows patchy, convective precipitation, much like that observed by Kirshbaum and Durran (2005b) or Nagle and Serebreny (1962) in post-frontal conditions. The locations of these transient, propagating convective cells vary over the course of the simulation, which highlights the need for longer averaging periods and multiple versions of the post-frontal simulations to obtain smoother precipitation fields that match more closely with the mean observed

distribution.

3.4 Results

3.4.1 Comparison with observations

The mean hourly precipitation distribution for the control simulations are presented next to the corresponding mean observed frontal periods from Chapter 2 in Figure 3.6. The magnitude and distribution of precipitation in the simulations and observations are similar for each frontal class and many of the differences between the frontal classes discussed in Chapter 2 are also evident in the simulations. All simulations exhibit an orographic enhancement of precipitation, especially on the southwest facing slopes of the Olympics. *ws-control* exhibits the greatest orographic enhancement of precipitation. The area in which precipitation is enhanced extends further upstream for *wf-control* compared to *ws-control*. The magnitude of precipitation in the whole domain is much smaller for *pf-control* than *wf-control* or *ws-control*.

However, there are some features of the simulations that do not appear in the observations. There is a significant downstream shift in the maxima of precipitation, which are now located over the northern peaks of the Olympics in all simulations. It is not clear if this is an artefact of the simulations or if this feature is missing from the observed distribution because of the bias correction technique that relies on gauges that are placed in valleys or relatively low ground (see gauge locations in Figure 2.1).

The *pf-control* and observed distributions differ in several ways. *pf-control* exhibits an enhancement upstream of the mountain and on the windward slopes, but the maximum has shifted from the foot of the mountain (as it is in observations) to a northern peak. This maximum is located in an area of the domain where the radar beam is at a relatively high altitude in the atmosphere (approximately 3km, as shown in Figure 2.6), which may be overshooting the top of the convective clouds. Moreover, there are no gauges to correct the radar estimate in this area. There are also prominent maxima further south of the Olympics in the observed mean distribution, which are not present in the simulations. It is possible that these maxima are due to convection being triggered by the relatively

	\bar{U} ms ⁻¹	I kgm ⁻¹ s ⁻¹	R_{up} mmh ⁻¹	ϵ	AE mmh ⁻¹	DR	DR^*
wf-obs	21.7	525	1.87	1.12	8.58	0.255	0.0321
wf-control	17.7	549	1.54	1.22	11.4	0.192	0.0716
ws-obs	23.3	640	1.14	0.706	10.8	0.23	0.12
ws-control	18.4	639	0.993	0.717	12.1	0.208	0.115
pf-obs	11.3	139	0.328	2.46	1.59	0.187	0.0105
pf-control	8.79	141	0.161	2.27	1.1	0.112	0.0373

Table 3.2: Mean properties of observed and simulated frontal periods. wf-obs, ws-obs and pf-obs refer to the mean observed warm-frontal, warm-sector and post-frontal periods from Chapter 2, respectively.

small mountains directly south of the Olympics (as previously observed by Parsons and Hobbs (1983)) and these mountains are not included in the simulations. For these small mountains, smaller h leads to a smaller value of ϵ and possibly a greater orographic enhancement of precipitation. Finally, there is a considerably stronger rain shadow (less precipitation) to the lee of the Olympics in pf-control than in the observed post-frontal distribution. This relatively weak rain shadow in the observed distribution may be partly accounted for by the variable wind direction for observed post-frontal cases, which leads to the rain shadow being smoothed out. Furthermore, terrain downstream of the Olympics is likely to be triggering convection in the observations, and this terrain is omitted from the simulations.

Quantitative analysis of the simulated flows is performed using the same methods as in Section 2.5.1, using the idealized frontal soundings. The results of this analysis are compared to the mean observed periods in Table 3.2. The values of I , U , R_{up} and ϵ , which we hypothesize are main controlling parameters for the resulting distribution of precipitation, match well with observations. AE and DR^* are the largest for ws-control and considerably smaller for pf-control, as with observations. The simulations show similar trends in both DR and DR^* as the observations. DR provides very little insight because it does not reflect the qualitative differences in the precipitation fields between different synoptic classes. DR^* varies considerably more between synoptic classes.

Table 3.2 supports the result from Chapter 2 that ϵ greatly influences the distribution of precipitation. Larger values of ϵ (which may be due to the presence of a stable layer in the lower atmosphere or weak winds) are correlated with smaller values of AE , DR , DR^*

and hence less absolute and relative orographic enhancement of precipitation. There is also more evidence for blocked flow in wf-control (Figure 3.6(a)) than ws-control (Figure 3.6(c)) in that there is a larger area upstream of the mountain in which the precipitation is enhanced. To see this more clearly, Figure 3.7 shows the control simulations with R_{up} subtracted from the whole precipitation field. Figure 3.7(a) exhibits a larger area of light blue (enhanced precipitation) upstream of the mountain than 3.7(b). pf-control (Figure 3.7(c)) exhibits some enhancement of precipitation in an area further upstream of the Olympics than ws-control, but this is not as prominent as with wf-control. The observations of post-frontal periods exhibited a maximum at the foot of the Olympics, which is consistent with blocked flow (and large ϵ), but this maximum has shifted downstream in the pf-control simulations.

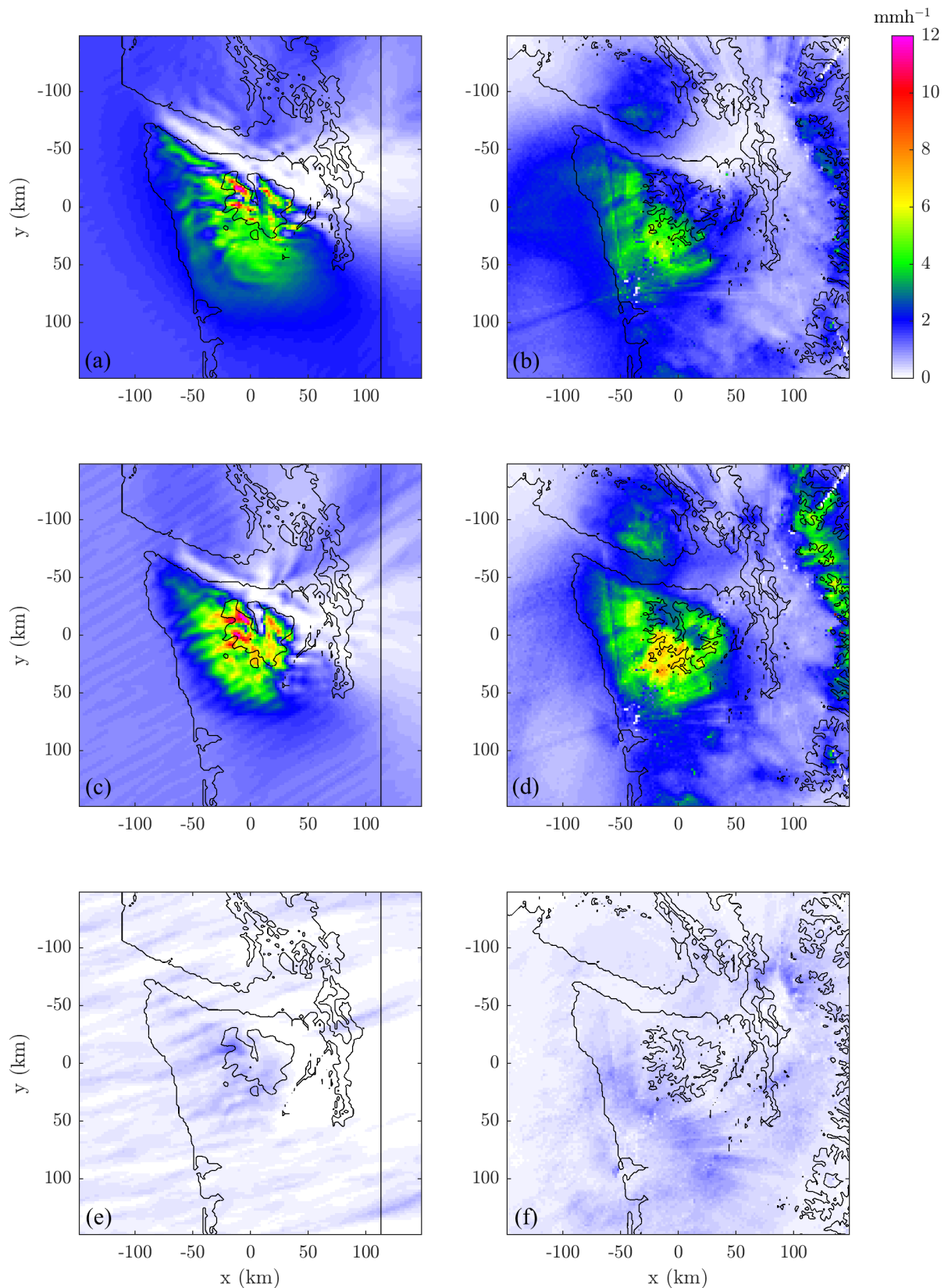


Figure 3.6: Mean hourly precipitation distribution for simulated (left column) and observed (right column) frontal periods over the Olympics. This data is obtained from (a) the wf-control simulations, (b) the warm-frontal observations, (c) the ws-control simulation, (d) the warm-sector observations, (e) the pf-control simulations and (f) the post-frontal observations. Figures (b), (d) and (f) are the same as Figures 2.12(a) (b) and (c), respectively.

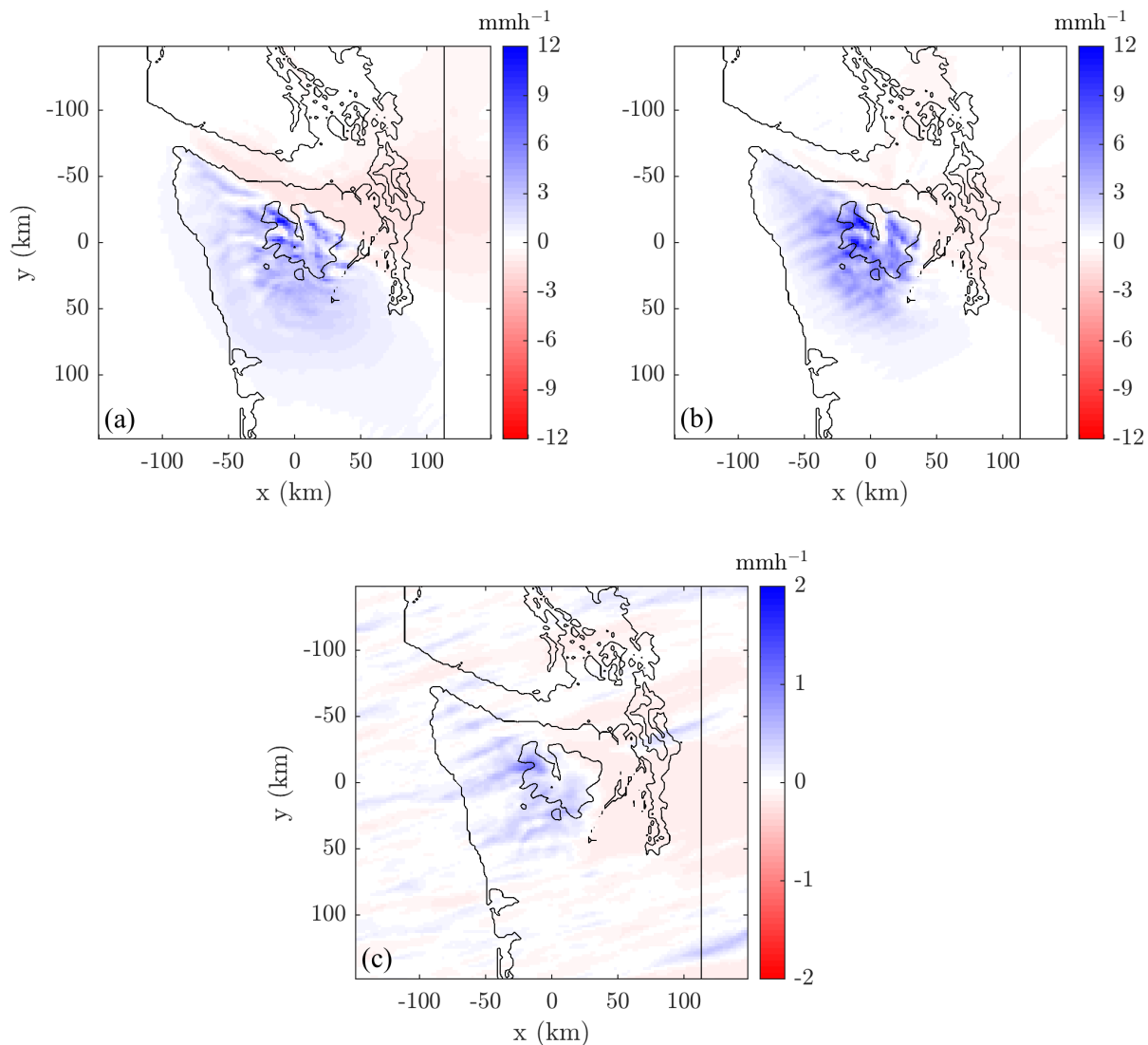


Figure 3.7: Mean upstream precipitation (R_{up}) subtracted from the mean precipitation distributions for (a) wf-control, (b) ws-control and (c) pf-control.

3.4.2 Sensitivity to upstream precipitation

Sensitivity to R_{up} is tested indirectly by varying w_{max} in the warm-frontal and warm-sector simulations or turning on and off surface fluxes and advective cooling for the post-frontal simulations. As can be seen in Figures 3.8(a)-(f), Figure 3.9 and Table 3.3, the presence of upstream precipitation makes a crucial difference to the precipitation distributions in the warm-frontal, warm-sector and post-frontal simulations.

The warm-frontal and warm-sector simulations with $R_{up} > 0$ ($w_{max} > 0$) have a significantly larger AE , DR and DR^* than the corresponding $R_{up} = 0$ simulations, which also do not look similar to the observed frontal periods (i.e. Figures 3.6 (b) and (d)). By comparing Figures 3.8(a) and (b) with 3.7(a) and (b) respectively, it is clear that

	w_{max} ms ⁻¹	\bar{U} ms ⁻¹	I kgm ⁻¹ s ⁻¹	R_{up} mmh ⁻¹	ϵ	AE mmh ⁻¹	DR	DR^*
wf-obs	-	21.7	525	1.87	1.12	8.58	0.255	0.0321
wf-wm0	0	17.7	549	0	1.22	3.3	0.0284	0.0284
wf-wm0.2	0.2	17.7	549	1.07	1.22	9.9	0.159	0.076
wf-control	0.3	17.7	549	1.54	1.22	11.4	0.192	0.0716
ws-obs	-	23.3	640	1.14	0.706	10.8	0.23	0.12
ws-wm0	0	18.4	639	0	0.717	8.93	0.0649	0.0649
ws-control	0.2	18.4	639	0.993	0.717	12.1	0.208	0.115
ws-wm0.3	0.3	18.4	639	1.53	0.717	12.8	0.25	0.107
pf-obs	-	11.3	139	0.328	2.46	1.59	0.187	0.0105
pf-noflux	-	8.79	141	0	2.27	6.26	0.0422	0.0422
pf-control	-	8.79	141	0.161	2.27	1.1	0.112	0.0373

Table 3.3: The same as in Table 3.2 but with properties from the additional simulations outlined in Table 3.1.

the addition of upstream precipitation does not simply augment the precipitation evenly over the whole domain. The upstream precipitation causes an uneven enhancement of precipitation in a large area in the vicinity of the Olympics, which is evidenced by the large area of blue in Figures 3.7(a) and (b) in comparison to the relatively confined area of precipitation in Figures 3.8(a) and (b). This highlights the importance of including R_{up} for realistically simulating orographic precipitation during warm-frontal and warm-sector conditions and hence also the importance of the seeder-feeder mechanism.

Whilst there is a large difference in DR^* between $w_{max} = 0$ and $w_{max} > 0$ simulations, DR^* actually decreases slightly from the $w_{max} = 0.2$ to the $w_{max} = 0.3$ simulations and there is only a modest increase in AE . Qualitatively, there are also only modest differences in the distribution and enhancement of precipitation between the $w_{max} = 0.2$ (Figures 3.8(c) and (d)) and the $w_{max} = 0.3$ simulations (Figures 3.8(e) and (f)). These results indicate that the mountain becomes less efficient at producing an enhancement of precipitation as R_{up} increases for warm-frontal and warm-sector simulations, but more simulations are needed with w_{max} varied incrementally to support this hypothesis.

Much like for warm-frontal and warm-sector, the pf-noflux simulations (Figure 3.9) do not look similar to the observed post-frontal periods (Figure 3.6(f)) despite the closely matching upstream parameters. However, unlike the warm-frontal and warm-sector simulations, AE and DR^* actually decrease from the $R_{up} = 0$ (pf-noflux) simulations to the $R_{up} > 0$ simulations (pf-control), which indicates that the influence of R_{up} is more compli-

cated in post-frontal conditions. In the pf-noflux simulations, there are quasi-stationary rain bands that persist over the mountain, which are not evident in the pf-control simulations. This is due to convective cells that develop upstream of the mountain in the pf-control case, which disrupt the flow and hinder the development of quasi-stationary rain bands (Kirshbaum and Durran, 2005a,b). The persistence of these rain bands in comparison to the scattered nature of precipitation during pf-control simulations, leads to a greater AE and DR^* .

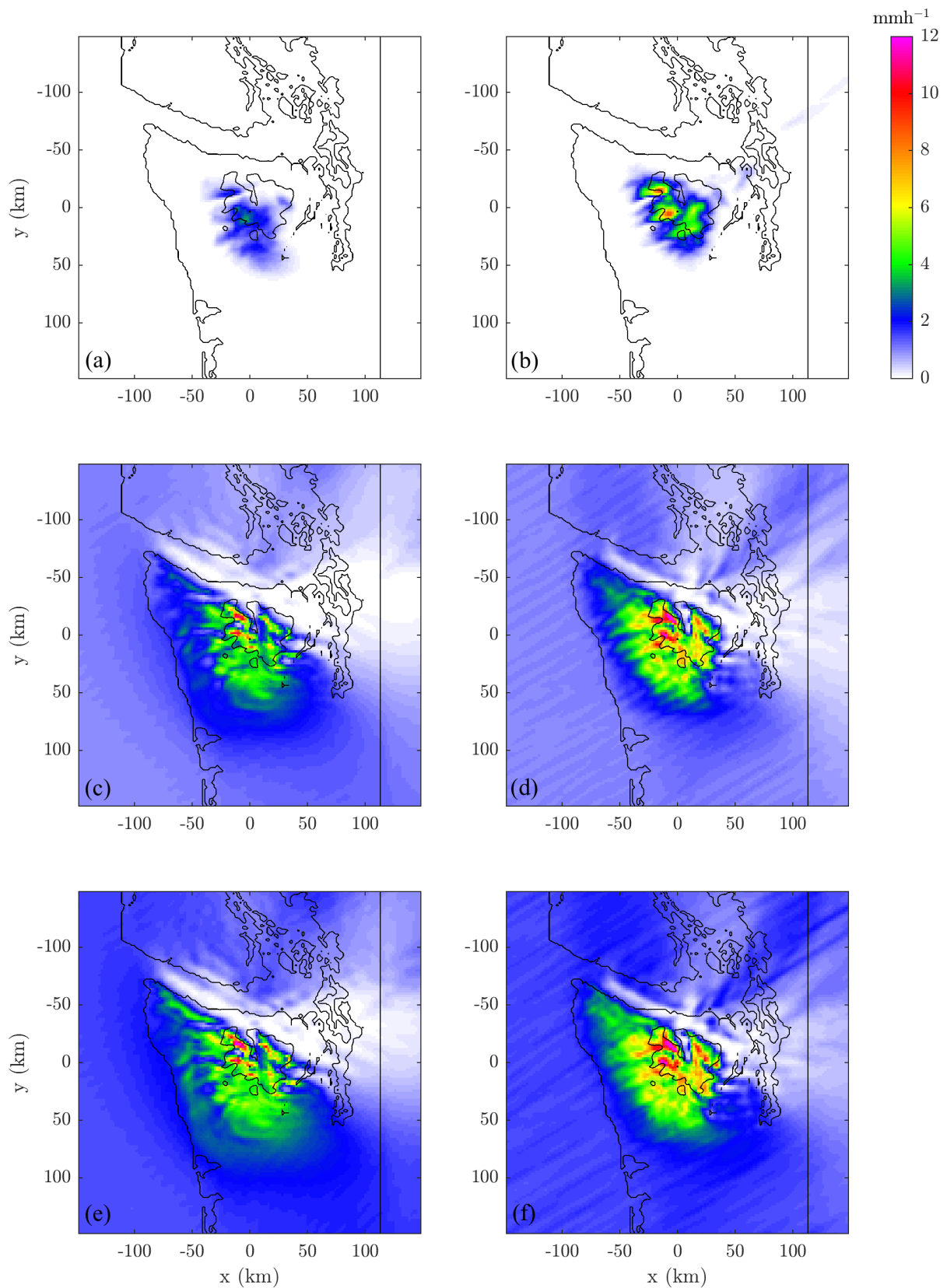


Figure 3.8: Mean hourly precipitation distribution for warm-frontal and warm-sector simulations with varying values of w_{max} . The figures are ordered such that $w_{max} = 0 \text{ms}^{-1}$ for the top row with (a) wf-wm0 and (b) ws-wm0, $w_{max} = 0.2 \text{ms}^{-1}$ for the middle row with (c) wf-wm0.2 and (d) ws-control, and $w_{max} = 0.3 \text{ms}^{-1}$ for the bottom row with (e) wf-control and (f) ws-wm0.3.

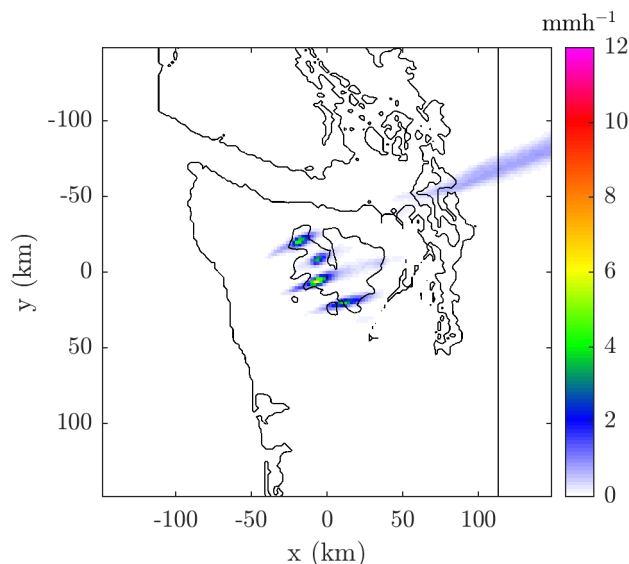


Figure 3.9: Mean hourly precipitation distribution for the pf-noflux simulations.

3.5 Discussion

We have used quasi-idealized simulations of frontal periods over the Olympics terrain that are based on observations from OLYMPEX to enhance the physical interpretation and support our results from Chapter 2. Importantly, we have considered the orographic enhancement of precipitation in the context of large-scale precipitation in different frontal sectors.

The control simulations were designed such that the upstream flow properties match closely with the mean observed frontal periods from Chapter 2 and they produced key qualitative and quantitative similarities to the observed precipitation distributions. All simulations produce an orographic enhancement of precipitation, especially on the south-west facing slopes, but the post-frontal simulations produce significantly less precipitation in comparison to the other frontal classes. The orographic enhancement is the largest for the warm-sector periods, but the area in which the precipitation was enhanced extended further upstream for warm-frontal periods than warm-sector periods. However, there are some clear discrepancies between the simulations and observations, especially on the north and northeastern (lee-side) peaks of the Olympics, where the simulations show local maxima in precipitation that are not present in the observations. Whilst some of the differences are likely to stem from the idealized nature of the simulations, others may originate in uncertainties of the observations, especially over the northern peaks of

the Olympics, where the radar measurements are above the freezing level (or possibly overshooting the top of the cloud in the post-frontal precipitation) and being corrected by sparse gauge measurements that are placed in valleys.

As with observations, the utility of DR^* over DR has been highlighted in our quantitative analysis of the simulations. DR is invariant despite large qualitative differences in the simulated distributions. Whereas, DR^* varies greatly between frontal classes and it appears to be inversely correlated with ϵ .

The increased ϵ in the warm-frontal simulations in comparison to the warm-sector simulations is due to the presence of a stable inversion in the lower part of the atmosphere. The stable inversion causes an upstream shift in the enhancement of precipitation and a decrease in the relative enhancement of precipitation over the mountain (smaller DR^*). Therefore, the stable inversion decreases the efficiency of warm-frontal periods in converting the incoming moisture flux to precipitation over the mountain. The observed post-frontal periods exhibited a maximum in precipitation at the foot of the mountain, which we hypothesized was because of flow blocking and this was consistent with large ϵ , but this result was not supported by our simulations. It is likely that this discrepancy is due to small mountains to the south of the Olympics that were omitted from simulations. These small mountains likely trigger convection (as observed by Parsons and Hobbs (1983)) because of smaller h , which then leads to a smaller ϵ and this permits flow to ascend these mountains more easily.

By comparing simulations with $R_{up} = 0$ and $R_{up} > 0$, we have found that R_{up} is a crucial factor for producing realistic simulations of orographic precipitation during frontal periods. The magnitude and distribution of precipitation over the mountain (and AE , DR and DR^*) is vastly different to observed cases with upstream conditions that closely match observations if $R_{up} = 0$. This highlights the importance of the seeder-feeder mechanism for the warm-frontal and warm-sector periods. In the post-frontal simulations with $R_{up} > 0$, the moist instability is constantly generated (by the surface fluxes and advective cooling) and then released (by convection) over the ocean, until it reaches land where there are no surface fluxes. Conversely, in the post-frontal simulations with $R_{up} = 0$ (pf-noflux), the moist instability is stored until the flow encounters the mountain, which

may lead to a greater orographic enhancement of precipitation, both absolute (AE) and relative (DR^*).

The comparison between warm-frontal and warm-sector simulations with $w_{max} = 0.2$ and $w_{max} = 0.3$ suggests that the mountain becomes less efficient at producing extra precipitation (smaller DR^*) as R_{up} increases, but more simulations are needed with w_{max} varied incrementally to test this hypothesis. These results contradict those reached by Bader and Roach (1977), who found that the magnitude of upstream precipitation greatly increased the enhancement of precipitation over the Welsh Hills in the UK. However, the Welsh Hills are much smaller in both height and horizontal extent than the Olympics, which makes them much less efficient at producing clouds and precipitation (because the perturbations produced by the mountain on the impinging flow are weaker). Precipitation is produced over the Olympics regardless of the presence of upstream precipitation (as shown in Figures 3.8(a), (b) and 3.9). Therefore, a stronger correlation between the magnitude of R_{up} and the orographic enhancement of precipitation is to be expected for the Welsh Hills in comparison to the Olympics.

Additional simulations have been run in order to test the robustness of our results by varying model parameters such as the microphysics scheme, the planetary boundary layer scheme and the spatial or temporal resolution being used. Initial results (not shown) are similar to those shown in this chapter. There are other factors that are not directly tested in our simulations which are undoubtedly important controlling factors for the distribution and orographic enhancement of precipitation. Namely, the vertical wind profile, temperature profile and the location of the 0°C isotherm, are only indirectly tested here. The warm-frontal and warm-sector wind and temperature profiles differ greatly from post-frontal profiles, but the mechanisms producing the precipitation are also different (i.e. large scale ascent as opposed to convective precipitation). Therefore, additional simulations are needed in which these factors are tested separately.

Chapter 4

Conclusions

Orographic precipitation distributions under varying synoptic conditions have been investigated in this study through observations and simulations over the Olympic Mountains.

A unique method for retrieving precipitation over the Olympics with radar and rain gauge data was outlined, using a combination of bias correction and optimal estimation techniques. The mean distribution of precipitation was then retrieved for six warm-frontal, warm-sector and post-frontal periods during OLYMPEX. All frontal periods produced an orographic enhancement of precipitation, especially on the southwest facing slopes of the Olympics. The warm-sector exhibited the greatest orographic enhancement of precipitation, both absolute (AE) and relative to the impinging moisture flux (DR^*). The area in which the precipitation was enhanced extended further upstream of the mountain for warm-frontal than for warm-sector periods. Post-frontal periods exhibited a maximum at the foot of the mountain but the precipitation rate and AE was much smaller than for warm-frontal or warm-sector.

Quasi-idealized simulations of frontal periods over the Olympics terrain were outlined to support our results from observations. To produce upstream precipitation in warm-frontal and warm-sector simulations, a horizontally uniform lifting profile was applied over the domain. For the post-frontal simulations, a combination of surface fluxes and advective cooling was used to constantly generate moist instability, with random potential temperature perturbations used to trigger convection. The simulations were designed so that the upstream flow conditions closely matched the observations and many of the key features of the observed precipitation distributions were reproduced: all simulations

produced some orographic enhancement on the southwest facing slopes of the Olympics, the warm-sector simulations exhibited the greatest orographic enhancement, the area in which the precipitation was enhanced extended further upstream of the mountain for warm-frontal than warm-sector simulations and the post-frontal simulations exhibited much weaker precipitation than the other two classes. However there were some prominent features in the simulations that did not agree with the observations. Namely, there were local maxima over the north and northeastern peaks of the Olympics during all frontal simulations that were not present in observations.

Through our analysis of observations and simulations we consistently found that DR^* , which is the same as DR except that it considers R_{up} , was useful for representing the qualitative differences between the precipitation distributions. Conversely, DR tended to be invariant between frontal classes despite large qualitative differences.

Our results suggest that the nondimensional mountain height (ϵ) greatly influences the distribution of precipitation. Small ϵ is correlated with large DR^* . The warm-sector has the largest DR^* , which suggests that it is the most efficient at converting the incoming moisture to precipitation over the mountain and this is supported by the small ϵ . Conversely for warm-frontal periods, the relatively large ϵ , which is due to the presence of a stable inversion in the lower part of the atmosphere, causes the area in which precipitation is enhanced to shift upstream (relative to the warm-sector), and it also causes a smaller enhancement over the mountain (smaller DR^*). Post-frontal periods had the largest ϵ (due to weak winds) and the smallest DR^* , but the maximum at the foot of the mountain that was present in observations (which is consistent with blocked flow) shifted downstream in simulations.

We ran sensitivity tests with R_{up} and found that it is a crucial factor for simulating frontal periods. Simulations with $R_{up} = 0$ do not match the observed periods, despite other closely matching upstream conditions. In post-frontal simulations, the presence of convection upstream of the mountain hinders the development of quasi-stationary rain bands over the mountain, which we did not observe over the Olympics, but have been observed for example over the Oregon Coastal Range by Kirshbaum and Durran (2005b).

4.1 Future Work

We will investigate in more detail the dynamical and microphysical properties of the flow during simulations discussed in Chapter 3. By inspecting the structure of the low-level winds, we will assess the extent to which flow is being directed around the mountain as opposed to ascending it and use this analysis to support our discussion of ϵ . More simulations of warm-frontal and warm-sector periods with w_{max} varied incrementally will be compared in order to determine the dependence of R_{up} on AE , DR and DR^* . Comparisons of the vertical cloud structure between simulations will be insightful for our discussions R_{up} , especially in regards to the seeder-feeder effect during warm-frontal and warm-sector conditions. More observations of frontal periods is also a future priority, given that this would greatly strengthen our results.

Bibliography

- Anders, A. M., G. H. Roe, D. R. Durran, and J. R. Minder, 2007: Small-scale spatial gradients in climatological precipitation on the olympic peninsula. *Journal of Hydrometeorology*, **8** (5), 1068–1081, doi:10.1175/JHM610.1.
- Bader, M. J. and W. T. Roach, 1977: Orographic rainfall in warm sectors of depressions. *Quarterly Journal of the Royal Meteorological Society*, **103** (436), 269–280, doi:10.1002/qj.49710343605, URL <http://dx.doi.org/10.1002/qj.49710343605>.
- Berenguer, M. and I. Zawadzki, 2008: A study of the error covariance matrix of radar rainfall estimates in stratiform rain. *Weather and Forecasting*, **23** (6), 1085–1101, doi:10.1175/2008WAF2222134.1.
- Berenguer, M. and I. Zawadzki, 2009: A study of the error covariance matrix of radar rainfall estimates in stratiform rain. part ii: Scale dependence. *Weather and Forecasting*, **24** (3), 800–811, doi:10.1175/2008WAF222210.1.
- Bianchi, B., P. J. van Leeuwen, R. J. Hogan, and A. Berne, 2013: A variational approach to retrieve rain rate by combining information from rain gauges, radars, and microwave links. *Journal of Hydrometeorology*, **14** (6), 1897–1909, doi:10.1175/JHM-D-12-094.1.
- Brandes, E. A., 1975: Optimizing rainfall estimates with the aid of radar. *Journal of Applied Meteorology*, **14** (7), 1339–1345, doi:10.1175/1520-0450(1975)014<1339:OREWTA>2.0.CO;2.
- Browning, K. A., F. F. Hill, and C. W. Pardoe, 1974: Structure and mechanism of precipitation and the effect of orography in a wintertime warm sector. *Quarterly Journal of the Royal Meteorological Society*, **100** (425), 309–330, doi:10.1256/smsqj.42504.
- Buzzi, A., N. Tartaglione, and P. Malguzzi, 1998: Numerical simulations of the 1994 piedmont flood: Role of orography and moist processes. *Monthly Weather Review*, **126** (9), 2369–2383, doi:10.1175/1520-0493(1998)126<2369:NSOTPF>2.0.CO;2.
- Colle, B. A. and C. F. Mass, 1996: An observational and modeling study of the interaction of low-level southwesterly flow with the olympic mountains during coast iop 4. *Monthly Weather Review*, **124** (10), 2152–2175, doi:10.1175/1520-0493(1996)124<2152:AOAMSO>2.0.CO;2.
- Colle, B. A. and C. F. Mass, 2000: The 5–9 february 1996 flooding event over the pacific northwest: Sensitivity studies and evaluation of the mm5 precipitation forecasts. *Monthly Weather Review*, **128** (3), 593–617, doi:10.1175/1520-0493(2000)128<0593:TFFEOT>2.0.CO;2.
- Cookson-Hills, P., D. J. Kirshbaum, M. Surcel, J. G. Doyle, L. Fillion, D. Jacques, and S.-J. Baek, 2017: Verification of 24-hour quantitative precipitation forecasts over the

- pacific northwest from a high-resolution ensemble kalman filter system. *Weather and Forecasting*, doi:10.1175/WAF-D-16-0180.1, in press.
- Doviak, R. J. and D. S. Zrnić, 1993: 2 - electromagnetic waves and propagation. *Doppler Radar and Weather Observations (Second Edition)*, R. J. Doviak, , and D. S. Zrnić, Eds., Academic Press, San Diego, second edition ed., 10 – 29, doi:https://doi.org/10.1016/B978-0-12-221422-6.50007-3, URL <http://www.sciencedirect.com/science/article/pii/B9780122214226500073>.
- Doyle, J. D. and N. A. Bond, 2001: Research aircraft observations and numerical simulations of a warm front approaching vancouver island. *Monthly Weather Review*, **129** (5), 978–998, doi:10.1175/1520-0493(2001)129<0978:RAOANS>2.0.CO;2.
- Durrán, D. R. and J. B. Klemp, 1983: A compressible model for the simulation of moist mountain waves. *Monthly Weather Review*, **111** (12), 2341–2361, doi:10.1175/1520-0493(1983)111<2341:ACMFTS>2.0.CO;2.
- Fabry, F., 2015: *Radar estimation of precipitation*, 148–165. Cambridge University Press, doi:10.1017/CBO9781107707405.010.
- Ferber, G. K. and C. F. Mass, 1990: Surface pressure perturbations produced by an isolated mesoscale topographic barrier. part ii: Influence on regional circulations. *Monthly Weather Review*, **118** (12), 2597–2606, doi:10.1175/1520-0493(1990)118<2597:SPPPBA>2.0.CO;2.
- Fulton, R. and C. Kondragunta, 2002: Multisensor precipitation estimator - the future of wfo rainfall estimation has arrived. *NWS Hydrologic Program Managers Conference*.
- Fulton, R. A., J. P. Breidenbach, D.-J. Seo, D. A. Miller, and T. O'Bannon, 1998: The wsr-88d rainfall algorithm. *Weather and Forecasting*, **13** (2), 377–395, doi:10.1175/1520-0434(1998)013<0377:TWRA>2.0.CO;2.
- Goudenhoofdt, E. and L. Delobbe, 2009: Evaluation of radar-gauge merging methods for quantitative precipitation estimates. *Hydrology and Earth System Sciences*, **13** (2), 195–203, doi:10.5194/hess-13-195-2009.
- Hobbs, P. V., 1975: The nature of winter clouds and precipitation in the cascade mountains and their modification by artificial seeding. part i: Natural conditions. *Journal of Applied Meteorology*, **14** (5), 783–804, doi:10.1175/1520-0450(1975)014<0783:TNOWCA>2.0.CO;2.
- Hong, S.-Y., Y. Noh, and J. Dudhia, 2006: A new vertical diffusion package with an explicit treatment of entrainment processes. *Monthly Weather Review*, **134** (9), 2318–2341, doi:10.1175/MWR3199.1.
- Hou, A. Y., R. K. Kakar, S. Neeck, A. A. Azarbarzin, C. D. Kummerow, M. Kojima, R. Oki, K. Nakamura, and T. Iguchi, 2014: The global precipitation measurement mission. *Bulletin of the American Meteorological Society*, **95** (5), 701–722, doi:10.1175/BAMS-D-13-00164.1.
- Houze, R. A., 2012: Orographic effects on precipitating clouds. *Reviews of Geophysics*, **50**, doi:10.1029/2011rg000365.
- Houze, R. A. and P. V. Hobbs, 1982: Organization and structure of precipitating cloud systems. *Advances in Geophysics*, **24**.

- Houze, R. A., C. N. James, and S. Medina, 2001: Radar observations of precipitation and airflow on the mediterranean side of the alps: Autumn 1998 and 1999. *Quarterly Journal of the Royal Meteorological Society*, **127** (578), 2537–2558, doi:10.1002/qj.49712757804.
- Houze, R. A. and S. Medina, 2005: Turbulence as a mechanism for orographic precipitation enhancement. *Journal of the Atmospheric Sciences*, **62** (10), 3599–3623, doi:10.1175/JAS3555.1.
- Houze, R. A., L. A. McMurdie, W. A. Petersen, M. R. Schwaller, W. Baccus, J. Lundquist, C. Mass, B. Nijssen, S. A. Rutledge, D. Hudak, S. Tanelli, G. G. Mace, M. Poellot, D. Lettenmaier, J. Zagrodnik, A. Rowe, J. DeHart, L. Madaus, and H. Barnes, 2017: The Olympic Mountains Experiment (OLYMPEX). *Bulletin of the American Meteorological Society*, accepted.
- Jarvis, A., H. Reuter, A. Nelson, and E. Guevara, 2008: Hole-filled srtm for the globe version 4, available from the cgiar-csi srtm 90m database. URL (<http://srtm.csi.cgiar.org>).
- Jiang, Q., 2003: Moist dynamics and orographic precipitation. *Tellus: Series A*, **55** (4), 301 – 316.
- Jiang, Q. and R. B. Smith, 2003: Cloud timescales and orographic precipitation. *Journal of the Atmospheric Sciences*, **60** (13), 1543–1559, doi:10.1175/2995.1.
- Joss, J., A. Waldvogel, and C. G. Collier, 1990: *Precipitation Measurement and Hydrology*, 577–606. American Meteorological Society, Boston, MA, doi:10.1007/978-1-935704-15-7_39.
- Kirshbaum, D. J., G. H. Bryan, R. Rotunno, and D. R. Durran, 2007: The triggering of orographic rainbands by small-scale topography. *Journal of the Atmospheric Sciences*, **64** (5), 1530–1549, doi:10.1175/JAS3924.1.
- Kirshbaum, D. J. and D. R. Durran, 2005a: Atmospheric factors governing banded orographic convection. *Journal of the Atmospheric Sciences*, **62** (10), 3758–3774, doi:10.1175/JAS3568.1.
- Kirshbaum, D. J. and D. R. Durran, 2005b: Observations and modeling of banded orographic convection. *Journal of the Atmospheric Sciences*, **62** (5), 1463–1479, doi:10.1175/JAS3417.1.
- Kirshbaum, D. J. and A. L. M. Grant, 2012: Invigoration of cumulus cloud fields by mesoscale ascent. *Quarterly Journal of the Royal Meteorological Society*, **138** (669), 2136–2150, doi:10.1002/qj.1954, URL <http://dx.doi.org/10.1002/qj.1954>.
- Kirshbaum, D. J. and R. B. Smith, 2008: Temperature and moist-stability effects on midlatitude orographic precipitation. *Quarterly Journal of the Royal Meteorological Society*, **134** (634), 1183–1199, doi:10.1002/qj.274.
- Koistinen, J. and D. Michelson, 2002: Baltex weather radar-based precipitation products and their accuracies. *Boreal Env. Res.*, **7**, 253–263.
- Kummerow, C., W. Barnes, T. Kozu, J. Shiue, and J. Simpson, 1998: The tropical rainfall measuring mission (trmm) sensor package. *Journal of Atmospheric and Oceanic Technology*, **15** (3), 809–817, doi:10.1175/1520-0426(1998)015<0809:TTRMMT>2.0.CO;2.

- Lin, Y. and K. E. Mitchell, 2005: The NCEP Stage II/IV hourly precipitation analyses: development and applications. *Preprints, 19th Conf. on Hydrology, American Meteorological Society, San Diego, CA, 9-13 January 2005.*, paper 1.2.
- Mass, C. F. and G. K. Ferber, 1990: Surface pressure perturbations produced by an isolated mesoscale topographic barrier. part i: General characteristics and dynamics. *Monthly Weather Review*, **118 (12)**, 2579–2596, doi:10.1175/1520-0493(1990)118<2579:SPPPBA>2.0.CO;2.
- Medina, S. and R. A. Houze, 2003: Air motions and precipitation growth in alpine storms. *Quarterly Journal of the Royal Meteorological Society*, **129 (588)**, 345–371, doi:10.1256/qj.02.13, URL <http://dx.doi.org/10.1256/qj.02.13>.
- Medina, S., E. Sukovich, and R. A. H. Jr., 2007: Vertical structures of precipitation in cyclones crossing the oregon cascades. *Monthly Weather Review*, **135 (10)**, 3565–3586, doi:10.1175/MWR3470.1.
- Minder, J. R., D. R. Durran, G. H. Roe, and A. M. Anders, 2008: The climatology of small-scale orographic precipitation over the olympic mountains: Patterns and processes. *Quarterly Journal of the Royal Meteorological Society*, **134 (633)**, 817–839, doi:10.1002/qj.258, URL <http://dx.doi.org/10.1002/qj.258>.
- Molini, A., L. G. Lanza, and P. La Barbera, 2005: The impact of tipping-bucket rain-gauge measurement errors on design rainfall for urban-scale applications. *Hydrological Processes*, **19 (5)**, 1073–1088, doi:10.1002/hyp.5646, URL <http://dx.doi.org/10.1002/hyp.5646>.
- Nagle, R. E. and S. M. Serebreny, 1962: Radar precipitation echo and satellite cloud observations of a maritime cyclone1. *Journal of Applied Meteorology*, **1 (3)**, 279–295, doi:10.1175/1520-0450(1962)001<0279:RPEASC>2.0.CO;2.
- Neiman, P. J., F. M. Ralph, B. J. Moore, and R. J. Zamora, 2014: The regional influence of an intense sierra barrier jet and landfalling atmospheric river on orographic precipitation in northern california: A case study. *Journal of Hydrometeorology*, **15 (4)**, 1419–1439, doi:10.1175/JHM-D-13-0183.1.
- Neiman, P. J., F. M. Ralph, A. B. White, D. E. Kingsmill, and P. O. G. Persson, 2002: The statistical relationship between upslope flow and rainfall in california’s coastal mountains: Observations during caljet. *Monthly Weather Review*, **130 (6)**, 1468–1492, doi:10.1175/1520-0493(2002)130<1468:TSRBUF>2.0.CO;2.
- Neiman, P. J., F. M. Ralph, G. A. Wick, J. D. Lundquist, and M. D. Dettinger, 2008: Meteorological characteristics and overland precipitation impacts of atmospheric rivers affecting the west coast of north america based on eight years of ssm/i satellite observations. *Journal of Hydrometeorology*, **9 (1)**, 22–47, doi:10.1175/2007JHM855.1.
- NGS, 1990: U.s. national geodetic survey data sheet. Accessed: 2017-06-14, https://www.ngs.noaa.gov/cgi-bin/ds_mark.pr1?PidBox=SY1857, accessed: 2017-06-14.
- Ólafsson, H. and P. Bougeault, 1996: Nonlinear flow past an elliptic mountain ridge. *Journal of the Atmospheric Sciences*, **53 (17)**, 2465–2489, doi:10.1175/1520-0469(1996)053<2465:NFPAEM>2.0.CO;2.

- Parsons, D. B. and P. V. Hobbs, 1983: The mesoscale and microscale structure and organization of clouds and precipitation in midlatitude cyclones. ix: Some effects of orography on rainbands. *Journal of the Atmospheric Sciences*, **40** (8), 1930–1949, doi:10.1175/1520-0469(1983)040<1930:TMAMSA>2.0.CO;2.
- Passarelli, R. E. and H. Boehme, 1983: The orographic modulation of pre-warm-front precipitation in southern new england. *Monthly Weather Review*, **111** (5), 1062–1070, doi:10.1175/1520-0493(1983)111<1062:TOMOPW>2.0.CO;2.
- Peterson, T. C., L. O. Grant, W. R. Cotton, and D. C. Rogers, 1991: The effect of decoupled low-level flow on winter orographic clouds and precipitation in the yampa river valley. *Journal of Applied Meteorology*, **30** (3), 368–386, doi:10.1175/1520-0450(1991)030<0368:TEODLL>2.0.CO;2.
- Purdy, J. C., G. Austin, A. W. Seed, and I. Cluckie, 2005: Radar evidence of orographic enhancement due to the seeder feeder mechanism. *Meteorological Applications*, **12** (3), 199–206, doi:10.1017/S1350482705001672, URL <http://dx.doi.org/10.1017/S1350482705001672>.
- Reinecke, P. A. and D. R. Durran, 2008: Estimating topographic blocking using a froude number when the static stability is nonuniform. *Journal of the Atmospheric Sciences*, **65** (3), 1035–1048, doi:10.1175/2007JAS2100.1.
- Richard, E., N. Chaumerliac, J. F. Mahfouf, and E. C. Nickerson, 1987: Numerical simulation of orographic enhancement of rain with a mesoscale model. *Journal of Climate and Applied Meteorology*, **26** (6), 661–669, doi:10.1175/1520-0450(1987)026<0661:NSOOEO>2.0.CO;2.
- Seo, D.-J., 1998: Real-time estimation of rainfall fields using radar rainfall and rain gage data. *Journal of Hydrology*, **208** (1), 37 – 52, doi:http://dx.doi.org/10.1016/S0022-1694(98)00141-3, URL <http://www.sciencedirect.com/science/article/pii/S0022169498001413>.
- Seo, D.-J., J. Breidenbach, and E. Johnson, 1999: Real-time estimation of mean field bias in radar rainfall data. *Journal of Hydrology*, **223** (3–4), 131 – 147, doi:http://doi.org/10.1016/S0022-1694(99)00106-7.
- Sideris, I. V., M. Gabella, R. Erdin, and U. Germann, 2014: Real-time radar–rain-gauge merging using spatio-temporal co-kriging with external drift in the alpine terrain of switzerland. *Quarterly Journal of the Royal Meteorological Society*, **140** (680), 1097–1111, doi:10.1002/qj.2188.
- Siler, N. and D. Durran, 2016: What causes weak orographic rain shadows? insights from case studies in the cascades and idealized simulations. *Journal of the Atmospheric Sciences*, **73** (10), 4077–4099, doi:10.1175/JAS-D-15-0371.1.
- Sinclair, S. and G. Pegram, 2005: Combining radar and rain gauge rainfall estimates using conditional merging. *Atmospheric Science Letters*, **6** (1), 19–22, doi:10.1002/asl.85.
- Smith, B. L., S. E. Yuter, P. J. Neiman, and D. E. Kingsmill, 2010: Water vapor fluxes and orographic precipitation over northern california associated with a landfalling atmospheric river. *Monthly Weather Review*, **138** (1), 74–100, doi:10.1175/2009MWR2939.1.

- Smith, J. A. and W. F. Krajewski, 1993: A modeling study of rainfall rate-reflectivity relationships. *Water Resources Research*, **29** (8), 2505–2514, doi:10.1029/93WR00962, URL <http://dx.doi.org/10.1029/93WR00962>.
- Smith, P. L., 1990: *Precipitation Measurement and Hydrology: Panel Report*, 607–618. American Meteorological Society, Boston, MA, doi:10.1007/978-1-935704-15-7_40.
- Smith, R. B., Q. Jiang, M. G. Fearon, P. Tabary, M. Dorninger, J. D. Doyle, and R. Benoit, 2003: Orographic precipitation and air mass transformation: An alpine example. *Quarterly Journal of the Royal Meteorological Society*, **129** (588), 433–454, doi:10.1256/qj.01.212, URL <http://dx.doi.org/10.1256/qj.01.212>.
- Steenburgh, W. J. and C. F. Mass, 1996: Interaction of an intense extratropical cyclone with coastal orography. *Monthly Weather Review*, **124** (7), 1329–1352, doi:10.1175/1520-0493(1996)124<1329:IOAIEC>2.0.CO;2.
- Surcel, M., I. Zawadzki, and M. K. Yau, 2014: On the filtering properties of ensemble averaging for storm-scale precipitation forecasts. *Monthly Weather Review*, **142** (3), 1093–1105, doi:10.1175/MWR-D-13-00134.1.
- Thompson, G., P. R. Field, R. M. Rasmussen, and W. D. Hall, 2008: Explicit forecasts of winter precipitation using an improved bulk microphysics scheme. part ii: Implementation of a new snow parameterization. *Monthly Weather Review*, **136** (12), 5095–5115, doi:10.1175/2008MWR2387.1.
- Velasco-Forero, C. A., D. Sempere-Torres, E. F. Cassiraga, and J. J. Gómez-Hernández, 2009: A non-parametric automatic blending methodology to estimate rainfall fields from rain gauge and radar data. *Advances in Water Resources*, **32** (7), 986 – 1002, doi:<http://doi.org/10.1016/j.advwatres.2008.10.004>, weather Radar and Hydrology.
- WRCC, 2017: Western u.s. climate historical summaries. Accessed: 2017-04-23, <http://www.wrcc.dri.edu/Climsum.html>, accessed: 2017-04-23.
- Yang, D., B. E. Goodison, J. R. Metcalfe, V. S. Golubev, R. Bates, T. Pangburn, and C. L. Hanson, 1998: Accuracy of nws 8” standard nonrecording precipitation gauge: Results and application of wmo intercomparison. *Journal of Atmospheric and Oceanic Technology*, **15** (1), 54–68, doi:10.1175/1520-0426(1998)015<0054:AONSNP>2.0.CO;2.
- Zhu, Y. and R. E. Newell, 1998: A proposed algorithm for moisture fluxes from atmospheric rivers. *Monthly Weather Review*, **126** (3), 725–735, doi:10.1175/1520-0493(1998)126<0725:APAFMF>2.0.CO;2.